Revisiting the HD 21749 planetary system with stellar activity modelling

Tianjun Gan [1]★ Sharon Xuesong Wang,[1,2]★ Johanna K. Teske,[2]† Shude Mao,[1,3] Ward S. Howard,[4] Nicholas M. Law,[4] Natasha E. Batalha,[5] Andrew Vanderburg,[6]‡ Diana Dragomir,[7] Chelsea X. Huang,[8]§ Fabo Feng,[9] R. Paul Butler,[9] Jeffrey D. Crane,[2] Stephen A. Shectman,[2] Yuri Beletsky,[2] Avi Shporer,[8] Benjamin T. Montet,[10] Jennifer A. Burt [11] Adina D. Feinstein,[12]¶ Erin Flowers,[13]¶ Sangeetha Nandakumar,[14] Mauro Barbieri,[14] Hank Corbett,[4] Jeffrey K. Ratzloff,[4] Nathan Galliher,[4] Ramses Gonzalez Chavez,[4] Alan Vasquez,[4] Amy Glazier[4] and Joshua Haislip[4]

[1]*Department of Astronomy and Tsinghua Centre for Astrophysics, Tsinghua University, Beijing 100084, China*
[2]*Observatories of the Carnegie Institution for Science, 813 Santa Barbara Street, Pasadena, CA 91101, USA*
[3]*National Astronomical Observatories, Chinese Academy of Sciences, 20A Datun Road, Chaoyang District, Beijing 100012, China*
[4]*Department of Physics and Astronomy, University of North Carolina at Chapel Hill, Chapel Hill, NC 27599-3255, USA*
[5]*NASA Ames Research Center, Moffett Field, CA 94035, USA*
[6]*Department of Astronomy, University of Wisconsin–Madison, Madison, WI 53706, USA*
[7]*Department of Physics and Astronomy, University of New Mexico, 1919 Lomas Blvd NE, Albuquerque, NM 87131, USA*
[8]*Department of Physics and Kavli Institute for Astrophysics and Space Research, Massachusetts Institute of Technology, Cambridge, MA 02139, USA*
[9]*Earth & Planets Laboratory, Carnegie Institution of Washington, 5241 Broad Branch Road, N.W., Washington, DC 20015, USA*
[10]*School of Physics, University of New South Wales, Sydney, NSW 2052, Australia*
[11]*Jet Propulsion Laboratory, California Institute of Technology, 4800 Oak Grove Drive, Pasadena, CA 91109, USA*
[12]*Department of Astronomy and Astrophysics, University of Chicago, 5640 S. Ellis Ave, Chicago, IL 60637, USA*
[13]*Department of Astrophysical Sciences, Princeton University, Princeton, NJ 08544, USA*
[14]*INCT, Universidad De Atacama, calle Copayapu 485, Copiapó, 1532297, Atacama, Chile*

ABSTRACT

HD 21749 is a bright ($V = 8.1$ mag) K dwarf at 16 pc known to host an inner terrestrial planet HD 21749c as well as an outer sub-Neptune HD 21749b, both delivered by Transiting Exoplanet Survey Satellite (*TESS*). Follow-up spectroscopic observations measured the mass of HD 21749b to be $22.7 \pm 2.2 \, M_\oplus$ with a density of $7.0^{+1.6}_{-1.3}$ g cm^{-3}, making it one of the densest sub-Neptunes. However, the mass measurement was suspected to be influenced by stellar rotation. Here, we present new high-cadence PFS RV data to disentangle the stellar activity signal from the planetary signal. We find that HD 21749 has a similar rotational time-scale as the planet's orbital period, and the amplitude of the planetary orbital RV signal is estimated to be similar to that of the stellar activity signal. We perform Gaussian process regression on the photometry and RVs from HARPS and PFS to model the stellar activity signal. Our new models reveal that HD 21749b has a radius of $2.86 \pm 0.20 \, R_\oplus$, an orbital period of 35.6133 ± 0.0005 d with a mass of $M_b = 20.0 \pm 2.7 \, M_\oplus$ and a density of $4.8^{+2.0}_{-1.4}$ g cm^{-3} on an eccentric orbit with $e = 0.16 \pm 0.06$, which is consistent with the most recent values published for this system. HD 21749c has an orbital period of 7.7902 ± 0.0006 d, a radius of $1.13 \pm 0.10 \, R_\oplus$, and a 3σ mass upper limit of $3.5 \, M_\oplus$. Our Monte Carlo simulations confirm that without properly taking stellar activity signals into account, the mass measurement of HD 21749b is likely to arrive at a significantly underestimated error bar.

Key words: stars: individual: HD 21749 – planetary systems.

1 INTRODUCTION

After the first discovery of a transiting planet HD 209458b (Charbonneau et al. 2000; Henry et al. 2000), the field of exoplanet research

★ E-mail: gtj18@mails.tsinghua.edu.cn (TG);
sharonw@mail.tsinghua.edu.cn (SXW)
† NASA Hubble Fellow.
‡ NASA Sagan Fellow.
§ Juan Carlos Torres Fellow.
¶ NSF Graduate Research Fellow.

entered a new chapter. The success of ground-based transit surveys such as HATNet (Bakos et al. 2004), SuperWASP (Pollacco et al. 2006), and KELT (Pepper et al. 2007, 2012) led to the detections of many giant planets (Collier Cameron et al. 2007; Penev et al. 2013). Later space missions including *CoRoT* (Baglin et al. 2006), *Kepler* (Borucki et al. 2010), and *K2* (Howell et al. 2014) produced an increasing number of terrestrial planets with well-measured radii which in turn enabled the detection of a bimodal distribution of planet radii occurrence rate (Fulton et al. 2017). Using measurements from the radial velocity method that constrains planet masses, planet densities, and compositions can be further studied (e.g. Rogers 2015).

Even though more than 4000 exoplanets[1] have been detected, most of them are too faint for RV follow-up observations to determine their masses. The recently launched Transiting Exoplanet Survey Satellite (*TESS*; Ricker et al. 2014, 2015) could increase the population of exoplanets with well-measured radius and mass significantly, as *TESS* focuses on nearby bright stars ($V < 13$ mag) and performs an all-sky survey. During the primary mission, *TESS* is expected to discover $\sim 10^4$ planets (Sullivan et al. 2015; Huang et al. 2018), and more than 2000 candidates have been identified, which is already providing the community with a large sample of ideal targets for further RV mass measurement and atmospheric characterization with the upcoming *James Webb Space Telescope* (*JWST*; Gardner et al. 2006) and *Extremely Large Telescope* (*ELT*; Gilmozzi & Spyromilio 2007; de Zeeuw, Tamai & Liske 2014).

Accurate and precise mass measurement is critical for analysing the atmospheric profiles and elemental abundances via transmission or emission spectroscopy (e.g. Batalha et al. 2019) as well as for modelling planetary interior structures in some cases (e.g. Otegi et al. 2020). For example, the equation below shows the degeneracy between the planet mass M_p and the mean molecular weight μ (Seager & Sasselov 2000; Seager, Deming & Valenti 2009)

$$H = \frac{kT}{\mu \times g_p} \propto \frac{1}{\mu M_p}, \tag{1}$$

where g_p represents the surface gravity, and H and T are the scale height and temperature of the atmosphere, respectively. Indeed, the work by Batalha et al. (2019) found that, for warm Neptunes and Earth-sized planets, the quality of the measured planetary masses heavily dictates the accuracy and precision of the retrieved atmospheric parameters such as temperature and scale height.

However, stellar activity, often manifesting as stellar rotation signals, can cause large RV variations that pose challenges to accurate mass determination (Queloz et al. 2009; Howard et al. 2013; Pepe et al. 2013). Stellar activity may thus make it particularly challenging to characterize small planets ($R < 4R_\oplus$), whose RV signals are often on par with or even smaller than the signals induced by stellar activity. In recent years, Gaussian process (GP) regression has been widely used to account for the stellar activity signals in RVs, and GP regression has demonstrated success in teasing out the signals of small planets with RV amplitudes down to an order of magnitude smaller than the stellar activity (e.g. Grunblatt, Howard & Haywood 2015; Rajpaul et al. 2015; López-Morales et al. 2016).

The case of HD 21749 represents a somewhat extreme entanglement between stellar activity and planetary signals. This planetary system was first reported by Trifonov, Rybizki & Kürster (2019) and Dragomir et al. (2019, hereafter D19). The rotation period of the star around 30–40 d is very close to the planet's orbital period near 35 d. Previous successful cases of disentanglement using GP very often dealt with systems where the two signals operate on very different time-scales, typically with P_{planet} significantly smaller than P_{rot} (e.g. Haywood et al. 2014; Grunblatt et al. 2015; López-Morales et al. 2016; Dai et al. 2017). While D19 does not expect the RV signal of HD 21749b to be strongly affected by stellar variability, our new analyses in this work show that, very inconveniently, the RV amplitude of the stellar activity signal is probably similar to that of the planet. Here, we present an updated planet mass measurement of HD 21749b where we disentangle the planetary component from the stellar activity signal in the RVs.

This paper is organized as follows: In Section 2, we describe the key observational data on HD 21749 used in this work, including *TESS* photometry as well as HARPS and PFS RVs. We analyse all data at hand in Section 3 including a study of the stellar rotation and our modelling of the stellar activity and planetary signals. In Section 4, we use our Monte Carlo simulations to evaluate the robustness of our model. Section 5 presents our discussions about the prospects of atmospheric characterization of HD 21749b, including a search for additional planets. We conclude our findings in Section 6.

2 OBSERVATIONS

The *TESS* photometry and PFS archival RVs in this work are the same as used in D19, except that we choose to adopt the HARPS data from the RVBANK (Trifonov et al. 2020). We direct the readers to Trifonov et al. (2019) and D19 for a description of the HARPS observations. Here, we briefly describe the *TESS* photometry in Section 2.1 and the PFS observations in Section 2.3. We have collected 147 more RV data points with PFS since D19, and so our final RV data set consists of 283 RV points.

2.1 TESS photometry

The original 2-min images of HD 21749 were reduced by using the Science Processing Operations Center (SPOC) pipeline (Jenkins et al. 2016) developed at NASA Ames Research Center. Based on the results from Transit Planet Search (TPS; Jenkins 2002; Jenkins et al. 2017), HD 21749 was alerted on the MIT TESS Alerts portal[2] as a single-transit planet candidate (TOI 186.01). After recovering a second partial transit of HD 21749b near a momentum dump in the Sector 3 data and detecting a third full transit in Sector 4, D19 successfully confirmed the planetary nature of HD 21749b when combining *TESS* data with the observations from the High Accuracy Radial velocity Planet Searcher (HARPS; Mayor et al. 2003) and the Planet Finder Spectrograph (PFS; Crane, Shectman & Butler 2006; Crane et al. 2008, 2010). Furthermore, D19 also validated the inner Earth-sized planet HD 21749c (TOI 186.02) based on the data from previous three *TESS* Sectors [1,2,3]. The *TESS* light curve used in our analysis was extracted from the publicly available target pixel stamps using a simple photometric aperture with a customized pipeline (the same as the one in D19), which has not been corrected for the dilution or any instrumental systematic signals (see the third paragraph of Section 2.1 in D19)

We use the Box Least Square algorithm (BLS; Kovács, Zucker & Mazeh 2002) to search for additional potential transiting planets after smoothing the light curve with a median filter. We confirm the 35.6 and 7.8 d signals reported in D19. After masking out all these in-transit data, we do not find any other significant transit signals that exist in the current *TESS* data.

2.2 Evryscope-South

Evryscope-South, which is located at Cerro Tololo Inter-American Observatory in Chile (Law et al. 2015), also observed 29059 epochs of HD 21749 over the course of 2.46 yr. The two Evryscope facilities (North and South) are comprised of arrays of small telescopes that continuously image the entire accessible sky each night down to an airmass of two. Each facility has an instantaneous footprint of 8150 square degrees and a total coverage of 18 400 square degrees.

---

[1] https://exoplanetarchive.ipac.caltech.edu/.

[2] https://tess.mit.edu/alerts/.

Evryscope-South employs a 'ratchet' strategy that tracks the sky for 2 h before ratcheting back into the initial position and continuing observations. The system observes at 2 min cadence in g' (Law et al. 2015) at a pixel resolution of 13 arcsec pixel^{-1} for $\sim$6 h each night. The typical dark-sky limiting magnitude is $g' = 16$. Astrometry and background subtraction are performed for each 28.8 MPix image. Raw photometry is extracted with forced apertures at target coordinates, then differential photometry is applied as described in Ratzloff et al. (2019).

2.3 PFS high resolution spectroscopy

We observed HD 21749 with PFS on the 6.5-m Magellan II Clay telescope at Las Campanas Observatory in Chile starting in 2010 January, about three months after PFS's first light, as part of the PFS long-term survey program to search for planets around nearby stars (e.g. Teske et al. 2016; Feng et al. 2019a). The work in D19 includes RVs from PFS taken until 2018 December 14 (BJD 2458476.6).

PFS is an environmentally controlled high-resolution spectrograph that uses an iodine cell for calibration to produce high-precision RVs. The spectral reduction and RV extraction for PFS data are performed with a custom IDL pipeline that is capable of delivering RVs with $<1\,\mathrm{m\,s^{-1}}$ precision (Butler et al. 1996, 2019). PFS was upgraded in 2018 January with a large format CCD, and the default RV observations were switched to a mode with a narrower slit (0.3 arcsec; pre-upgrade mode was with a 0.5 arcsec slit). This increased the spectral resolution from $R \sim 80\,000$ to $R \sim 130\,000$ and led to an increase in RV precision. We denote the RV observations taken with the pre-upgrade PFS with 'PFSF' (before BJD 2458000) and the post-upgrade ones with 'PFSS'.

Starting 2018 October, HD 21749 was observed as one of the targets in the Magellan *TESS* Survey (MTS), which will characterize $\sim$30 *TESS* discovered super-Earths and sub-Neptunes to assemble a statistically robust sample of small planets (Teske et al. in preparation). Since D19, we have obtained 147 additional RV observations (53 epochs) as part of MTS.

The 42 PFSF RV observations were taken with a typical exposure time of 300 s, mostly one exposure per epoch (41 epochs), and a set of template observations (3 $\times$ 550-s exposures) were taken through the 0.3 arcsec slit with the pre-upgrade PFS without using the iodine cell. The 181 PFSS observations (62 epochs) consist of mostly pairs of two $\sim$300-s exposures, sometimes followed by another pair of observations a few hours later within the same night. This intra-night high cadence was designed to average out stellar jitter (Dumusque et al. 2011) and potential instrumental noise. In addition, the MTS observations on HD 21749 were executed with high cadence ($\sim$nightly visit when possible) in order to achieve good sampling on both the time-scale of the stellar rotation and that of the planetary orbit.

We also derive two spectroscopic activity indicators from the PFS data: the emission flux in the Ca II H & K lines (S_{HK}; Duncan et al. 1991) and the Hα line ($S_{H\alpha}$; Gomes da Silva et al. 2011), both residing in spectral regions free of iodine absorption lines. We perform the barycentric correction using Precise EXOplanetology (PEXO; Feng et al. 2019b). The PFS data used in this work are publicly available on ExoFOP–TESS.[3]
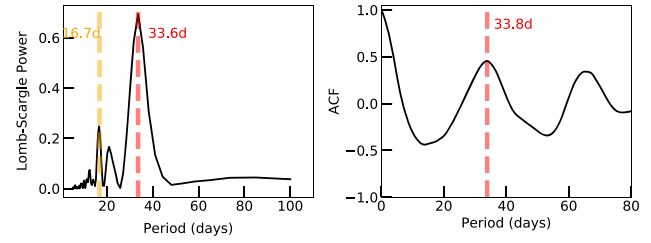
Figure 1. Left-hand panel: LS power spectrum of the systematics-corrected *TESS* light curve with the peaks marked by vertical dashed lines. Right-hand panel: Autocorrelation function (ACF) of the same data set. Both of them show a consistent rotation period $\sim$33 d (see Section 3.1).

3 ANALYSES AND RESULTS

In this work, we adopt the stellar radius $R_\star = 0.695 \pm 0.030\,\mathrm{R_\odot}$, mass $M_\star = 0.73 \pm 0.07\,\mathrm{M_\odot}$, and effective temperature $T_{\mathrm{eff}} = 4640 \pm 100$ K from D19. We encourage readers to refer to D19 for more details.

3.1 Stellar rotation

We first evaluate the evidence for the stellar rotation signal and determine the rotation period of HD 21749. We employ the Lomb–Scargle (LS) periodogram to perform the frequency analysis (Lomb 1976; Scargle 1982) and search for rotational spot modulation in the *TESS* photometry (Sector 1–Sector 4; baseline $\sim$110 d). For this analysis, we exclude the second segment of data in Sector 4 where it exhibits a sharp downturn between BJD = 2458420 and BJD = 2458424 (see the blue highlighted part in Fig. 6), possibly due to a series of events on board *TESS* including a camera shut-off and a heater turn-on, causing the PSF to change. We explore the period space between 5 and 100 d after masking out all transits. We find a prominent peak at $\sim$33.6 d (red dashed line in Fig. 1) which is close to the values reported in D19. A less significant peak located at $\sim$16.7 d, nearly half of the rotation period, is likely the second harmonic of the rotation signal (orange dashed line in Fig. 1). Following Gan et al. (2020), we compute the autocorrelation function (ACF) of the *TESS* light curve using Numpy.correlate (McQuillan, Aigrain & Mazeh 2013). The ACF exhibits a broad peak at $\sim$33.8 d, which again suggests the $\sim$33 d photometric signal could be the real rotation period of HD 21749 (see Fig. 1). We note that although there are systematic signals in the extracted *TESS* light curve (e.g. due to reaction wheel momentum dump events; Vanderburg et al. 2019) and an elevated noise in Sector 4, it is unlikely to have a relatively smooth systematic signal with such a long period ($\sim$33 d) and large amplitude (200–400 ppm). Therefore, we conclude that the $\sim$33 d signal is due to the stellar rotation.

A recent study from Canto Martins et al. (2020) reported a 66.8 d rotation period using Sections 1–3 of the *TESS* photometry spanning 88 d. This periodicity of 66.8 d is about twice the period of our finding, and we think it is a multiple of the true rotation period near 33 d. First, with an effective temperature of $T_{\mathrm{eff}} = 4640 \pm 100$ K and a stellar age of 3.8 ± 3.7 yr (D19), the mid-K dwarf HD 21749 is highly unlikely to have a rotation period $P_{\mathrm{rot}} > 60$ d according to gyrochronology (e.g. see fig. 5 in McQuillan, Mazeh & Aigrain 2014[4]; Barnes 2007; Mamajek & Hillenbrand 2008; Curtis et al.

---

[3]https://exofop.ipac.caltech.edu/tess/target.php?id = 279741379.

[4]McQuillan et al. (2014) used data from Kepler, where periods longer than $\sim$30 d were suppressed by PDC.
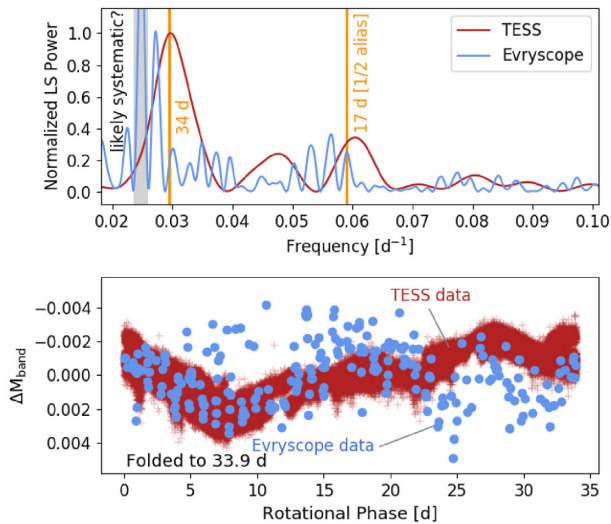
Figure 2. Top panel: Evryscope and *TESS* LS periodograms show power near 17 d. *TESS* also shows power at twice this period, ~34 d. A likely systematic period at 40.3 d is highlighted in grey. Bottom panel: The Evryscope and *TESS* light curves are phase-folded at a period of 33.9 d. The *TESS* amplitude is ~2 mmag, close to the detection limit of phase-folded Evryscope observations. Evryscope observations are binned in phase to increase the detectability. Variability of the same phase and amplitude as in *TESS* is observed at low signal to noise.

2019). Moreover, we detect a strong periodic signal around 31 d in the PFS magnetic activity indicators $S_{\rm HK}$ and $S_{\rm H\alpha}$ (see below), which suggests that HD 21749 is probably not a very old and slowly rotating star. Thus we conclude that this 66.8 d period is the $2P_{\rm rot}$ signal.

Additional ground-based photometry also supports this finding. We observe periodic variability at ~33.9 d (blue points in Fig. 2) with observations by Evryscope-South. We pre-whiten the light curve, iteratively removing likely systematics-affected periods including periods at 1, 51, 90, and 365 d. We then phase-fold the light curve to 33.9 d. Due to the low ~2 mmag amplitude, we bin the light curve in phase to increase the signal to noise. The Evryscope periodogram displays a series of peaks near the 1/2 alias of the ~33 d *TESS* signal but does not detect the ~33 d signal directly. Multiplying the clearest Evryscope signal at 16.97 d by two, we phase-fold the light curve at 33.9 d and observe a signal of similar amplitude and phase as in the *TESS* light curve as shown in Fig. 2. Other nearby periods do not match the *TESS* rotational phase as closely as the 16.97 d signal. We note that HD 21749 has a g' magnitude close to the non-linear regime of Evryscope. Furthermore, strong daily and yearly cycles are also present in the light curve prior to pre-whitening. These factors make our detection tentative but part of a cumulative case for an ~33–34 d period. The 40.3-d signal is likely an Evryscope systematic as it is similar to spurious periods seen in other light curves and does not correctly phase up the *TESS* light curve. More detail on the Evryscope light curve of HD 21749 is given in Howard et al. (in preparation).

Using photometric data from KELT (Pepper et al. 2007, 2012), Oelkers et al. (2018) derived a rotation period of 47.6 d for HD 21749, while D19 reported the tallest peak in the LS periodogram is at 38.95 d with the second tallest peak near 33 d. The relatively low precision and systematic noise, which commonly associated with ground-based photometry, prevent us from detecting the rotation period of HD 21749 in a statistically significant way. We prefer the $P_{\rm rot}$ value derived from the space photometry as *TESS* data has much higher precision.

We then derive the rotation period from the spectroscopic data. D19 constrained the rotation period to be 34.5 ± 7 d based on the $\log(R_{\rm HK})$ index (Mamajek & Hillenbrand 2008), and ~37 d based on the LS periodograms of HARPS activity indicators ($S_{\rm HK}$ and $S_{\rm H\alpha}$). Additionally, the rotation speed ($v\sin i \sim 1.04$ km s^{-1}) obtained from the HARPS spectra places a constraint on $P_{\rm rot}/\sin i$ around 33.8 d (D19). We search for periodic signals in the combined HARPS and PFS radial velocity data by utilizing the generalized Lomb–Scargle (GLS) periodogram (Zechmeister & Kürster 2009). A highest peak around 35.6 d is detected at the orbital period of the transiting planet HD 21749b. After subtracting the optimized Keplerian solution (described below), we do not find any other significant peaks. We further investigate the GLS periodogram of the stellar activity indicators: $S_{\rm HK}$ and $S_{\rm H\alpha}$ indices from PFS, as well as the chromatic RV index (CRX) and the differential line width (DLW) from HARPS. The activity indicators from the HARPS spectra were extracted by using the publicly available SpEctrum Radial Velocity AnaLyser pipeline (SERVAL; Zechmeister et al. 2018; Trifonov et al. 2020). Trifonov et al. (2019) mentioned that the strongest power in DLW is at lower frequencies, which is also true for $S_{\rm H\alpha}$ and $S_{\rm HK}$. After excluding an outlier ($S_{\rm H\alpha} = -1.0$), we find an obvious peak at around 31 d in the $S_{\rm HK}$ periodogram and a forest of peaks around 30 d in the $S_{\rm H\alpha}$ periodogram, which adds credence to the $P_{\rm rot}$ value inferred in the *TESS* light-curve analysis above. However, we do not find a significant peak in HARPS RV data that is consistent with the ~31 d rotation signal seen in $S_{\rm HK}$. This may be due to the relatively poor sampling on the time-scale of the stellar rotation. We show all our frequency analyses in Fig. 3. Both photometric and spectroscopic evidences show that $P_{\rm rot}$ is between 31 and 37 d. Thus, we choose to place a relatively wide uniform prior ([30, 40]) on $P_{\rm rot}$ in the following GP + transit modelling (see Section 3.2).

In order to determine whether the stellar rotation has a significant effect on the Doppler signals, we measure the Pearson's r correlation coefficients between the temporal series of RV and CRX, DLW. Fig. 4 shows the CRX and DLW as a function of RV. We find HARPS RVs have a weak anticorrelation ($r = -0.13$, p-value ~ 0.3) with CRX but a strong correlation ($r = 0.54$, p-value ~ 10^{-5}) with DLW. Clear correlations between RV and $S_{\rm HK}$, $S_{\rm H\alpha}$ are also found in the PFSS-only data ($r = 0.43$, p-value ~ 10^{-9}; $r = 0.38$, p-value ~ 10^{-7}), which suggests that we need to mitigate the stellar jitter caused by rotation (Fig. 5). Although D19 estimated that the stellar variability has a minor effect on the RV signals ($\sigma_{s,\rm RV} \approx 1.3$ m s^{-1}) based on the standard deviation of the *TESS* fluxes ($\sigma_{s, \rm TESS} \sim 0.0013$), our evaluation of the stellar activity of HD 21749 above prompted us to reanalyse this system. We show that the stellar activity has a $\sigma_{\rm pp,RV} \approx 6$ m s^{-1} contribution to the RV according to the peak-to-peak flux variation ($\sigma_{\rm pp, TESS} \sim 0.006$) in Section 3.3.

3.2 Fitting the transits and the stellar activity in *TESS* photometry

In order to constrain the stellar rotation period from photometrirc data directly, instead of fitting a basis spline to detrend the *TESS* light curve as in D19, we perform a joint fit of the light curve with a GP model using JULIET (Espinoza, Kossakowski & Brahm 2019). The transit model is created by BATMAN (Kreidberg 2015) while the GP is modelled using CELERITE (Foreman-Mackey et al. 2017). Dynamic nested sampling is performed using the public package DYNESTY (Higson et al. 2019; Speagle 2020).

Though *TESS* has high photometric precision, light contamination from nearby stars is of concern due to its large pixel scale (21 arcsec per pixel, Ricker et al. 2014), which could pollute the aperture. To
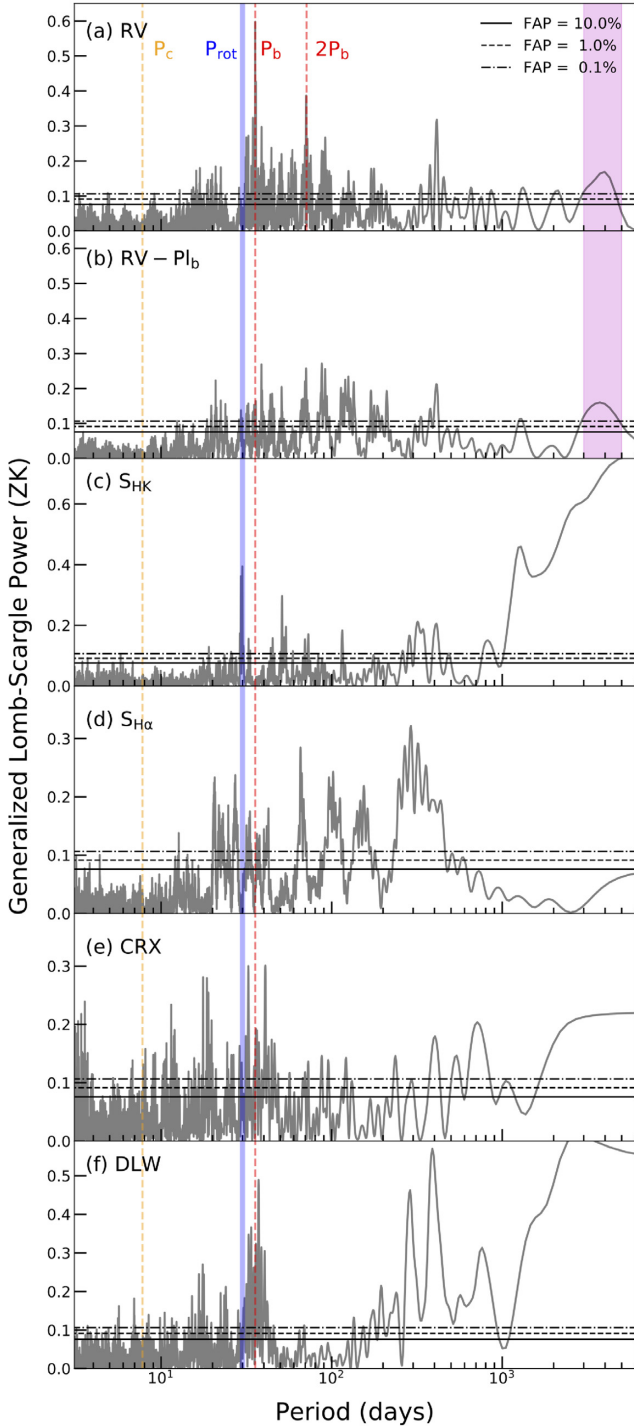
Figure 3. GLS periodograms of: (a) Combined HARPS and PFS radial velocity data (after adjusting for the RV offsets between different instruments using the best-fitting values in our GP + 1pl model presented in Section 3.3). (b) Combined HARPS and PFS radial velocity data after subtracting the best-fitting Keplerian model of HD 21749b. (c and d) PFS stellar activity indicators S_{HK} and $S_{H\alpha}$. (e and f) HARPS stellar activity indicators CRX and DLW. The orbital periods of HD 21749b and the planet candidate HD 21749c are shown as red and orange vertical dashed lines, respectively. The shaded vertical region represents the signal of a potential outer planet companion (see Section 5.2). The stellar rotation period 31 d derived from the spectroscopy data is shown as blue vertical lines. The theoretical FAP levels of 10, 1, and 0.1 per cent are marked as horizontal solid, dashed, and dot–dashed lines.
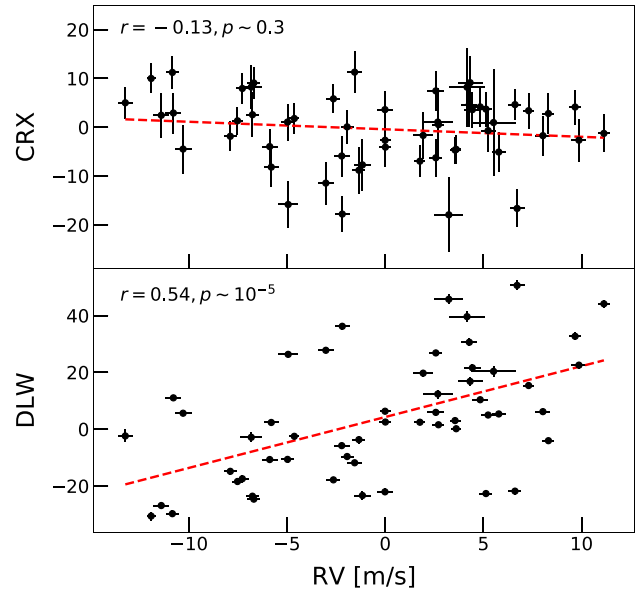
Figure 4. Chromatic RV index (CRX) and differential line width (DLW) as a function of HARPS RV with the Pearson's correlation indexes and p-values shown on the upper left. The correlation fits are shown as red dashed lines. The correlation between DLW and RV indicates that the stellar activity has an effect on the HARPS Doppler signals (see Section 3.1).
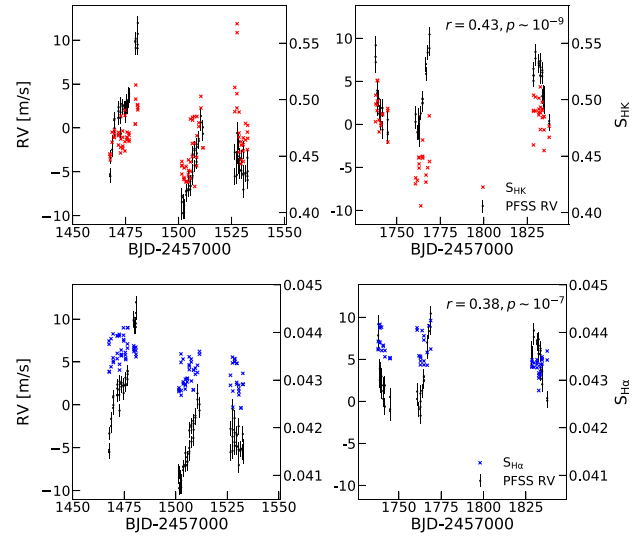
Figure 5. Top panels: RV and stellar activity indicator S_{HK} versus time for PFSS only data. Bottom panels: RV and $S_{H\alpha}$ versus time. The Pearson's correlation indexes and the corresponding p-values are shown on the upper right. The clear similar trend of RV and S_{HK}, $S_{H\alpha}$ makes the stellar rotation influence require particular care.

correct the flux dilution effect, **juliet** enables one to fit a model with the form

$$\mathcal{M}(t) = [\mathcal{T}(t)D + (1 - D)] \left(\frac{1}{1 + D \cdot M} \right), \qquad (2)$$

where $\mathcal{M}(t)$ and $\mathcal{T}(t)$ represent the photometric and transit models while D and M are the dilution factor and mean offset out-of-transit flux, respectively. We search the nearby stars of HD 21749 ($G_{rp} = 6.95$) within 1 arcsec in the *Gaia* DR2 (Gaia Collaboration 2018)

to estimate the flux dilution factor D_{TESS} in the *TESS* photometry. A relatively bright giant star (*Gaia* DR2 4673947071237511552, $G_{rp} = 9.05$) 22 arcsec away is expected to have a significant contribution to the contaminated flux while three faint neighbours located at >35 arcsec with $G_{rp} \gtrsim 16.0$ have essentially no measurable effect. As the *Gaia* G_{rp} band and the *TESS* band are similar, we simply evaluate the $D_{TESS} \approx 0.87$ using equation (6) in Espinoza et al. (2019)

$$D = \frac{1}{1 + \sum_n F_n/F_T}, \qquad (3)$$

where F_T and F_n represent the flux of target and contamination sources. This value is consistent with 0.8605, the one reported in the *TESS* Input Catalog (TIC) V8 (Stassun et al. 2018, 2019). Hence, we set a Gaussian prior on D_{TESS} during the joint-fit based on the estimate above with the width $\sigma = 0.01$. In addition, instead of directly fitting for the planet-to-star radius ratio ($R_P/R_\star$), orbital inclination (i), and scaled separation distance ($a/R_\star$), we sample points using the new parametrizations r_1 and r_2 to keep all values physically plausible (Espinoza 2018). Because of the weak constraint on eccentricity from photometric data alone, we assume circular orbits for both HD 21749b and HD 21749c, place a non-informative log-uniform prior on stellar density and fix the orbital eccentricity to zero in our transit fit. We apply the quadratic limb-darkening law and sample the coefficients (q_1 and q_2) between 0 and 1 uniformly as described in Kipping (2013). We include a flux jitter term σ_{TESS} to describe the additional white noise in the *TESS* photometry.

To model the photometric variations in the *TESS* light curve, we use GP regression with a rotation kernel formulated by Foreman-Mackey et al. (2017)

$$k_{i,j}(\tau) = \frac{B}{2+C} e^{-\tau/L} \left[\cos\left(\frac{2\pi\tau}{P_{rot}}\right) + (1+C) \right], \qquad (4)$$

where B defines the GP covariance amplitude, C is a balance parameter for the periodic and the non-periodic parts, $\tau = |t_i - t_j|$ is the time-lag between data point i and j, and L and P_{rot} represent the coherence time-scale and the stellar rotational period, respectively. We adopt uninformative, wide log-uniform priors to the GP parameters except for the periodic time-scale P_{rot}, where we choose a relatively narrow uniform prior between 30 and 40 d according to our findings in Section 3.1. We find a best fit of $P_{rot} = 31.2 \pm 1.5$ d and a radius of $2.86 \pm 0.20\,R_\oplus$ in the GP + transit joint fit, combined with the stellar radius $R_\star = 0.695 \pm 0.030\,R_\odot$ taken from D19. We note that D19 was published before TICv8 came out thus it used the original dilution value from TICv7. Our radius estimate here is larger than the radius of $2.61^{+0.17}_{-0.16}\,R_\oplus$ reported by D19 due to an updated dilution factor in this work (TICv8). In addition, combined with the stellar effective temperature $T_{eff} = 4640 \pm 100$ K retrieved from D19, assuming albedo is equal to 0, we find HD 21749b and HD 21749c have an equilibrium temperature of 407 ± 22 and 676 ± 36 K, respectively.

As mentioned in Section 3.1, the second segment in Sector 4 might be subject to strong systematic noise, and thus we exclude this feature so that it does not bias our estimate of P_{rot}. Therefore, we fit a GP-only model to the *TESS* photometry after excluding that abnormal part and masking out all transits, and we obtain $P_{rot} = 31.7 \pm 3.4$ d, consistent with our current findings in the GP + transit joint fit. We list the best-fitting parameters and the corresponding prior settings in Table 1. The *TESS* light curve of HD 21749 along with the best-fitting GP + transit model is shown in Fig. 6. We present each transit of HD 21749b in Fig. 7.

3.3 RV modelling

We choose to fit the RVs independently of the transit fit with priors informed by the photometric analysis. To fit the RV measurements, **JULIET** utilizes the **RADVEL** algorithm to create the Keplerian orbit model (Fulton et al. 2018). We compare different RV models based on the Bayesian model log-evidence (ln Z) calculated by the **DYNESTY** package. Overall, we consider a model to be favoured if $\Delta \ln Z > 2$, and strongly supported if $\Delta \ln Z$ is greater than 5 (Trotta 2008; Luque et al. 2019).

3.3.1 1pl model for all data

First, the RV perturbation caused by HD 21749c is probably unmeasurable given the RV precision of our data set. We estimate the planet mass to be $1.5 \pm 0.5\,M_\oplus$ based on the empirical mass–radius relation from Chen & Kipping (2017), which corresponds to a radial velocity semi-amplitude K_c of ~ 0.6 m s^{-1}, assuming a circular orbit. This expected signal is beyond the detection limit of HARPS and PFS. Hence, we choose to exclude HD 21749c in our RV analysis and start with one planet (i.e. HD 21749b; 1pl for short) model fit (denoted as M1). For each instrument, we model the RV offset and the RV jitter term accounting for additional white noise independently. We fix the RV slope and quadratic terms[5] equal to 0 and free $e\sin\omega$ and $e\cos\omega$ in all our runs. In this fit with a pure Keplerian model, we obtain $K_b = 6.11 \pm 0.37$ m s^{-1}, which agrees with the $5.51^{+0.41}_{-0.33}$ m s^{-1} value reported by D19 within 2σ. We note here that the error bar does not decrease considerably after adding 147 more PFSS RVs in this simple Keplerian fit, as one would expect in the case of white noise. This is probably because the newly added PFSS RVs contain highly correlated noise due to the existence of stellar activity sampled at high cadence.

3.3.2 GP + 1pl model for all data

However, as shown in Section 3.1, we find a clear correlation between the RV data points and the stellar activity indicators. This indicates that the RVs may have been influenced by stellar activity thus biasing the Keplerian fit. To estimate the RV variation induced by the stellar activity, we employ equation (2) in Vanderburg et al. (2016)

$$RV_{pp} \simeq F_{pp} \times v\sin i, \qquad (5)$$

where RV_{pp} and F_{pp} are the peak-to-peak variation of RV and flux, respectively.[6] We estimate the $v\sin i$ to be ~ 1.0 km s^{-1} based on the stellar radius and derived rotation period in Section 3.1 (again, consistent with the $v\sin i$ estimated from the HARPS spectra; Dragomir et al. 2019). The *TESS* light curve gives an $F_{pp} \sim 6$ ppt (parts per thousand), which translates into an ~ 6 m s^{-1} effect on the RVs. This estimated RV effect from the stellar activity is similar to the RV semi-amplitude of the planet orbit. Therefore, in order to make a robust mass estimation, we include a GP model accounting for the stellar activity signals and perform a GP + one planet (GP + 1pl; HD 21749b, M2) fit.

Adopting the assumption that both the light curve and the RV curve should have the same frequency structure in the covariance function representing the stellar activity, we take the posteriors of coherence

---

[5]We fix the RV slope and quadratic terms to zero because our model comparison using Bayesian evidence suggests that a model without such terms is strongly favoured ($\Delta \ln Z = 13$).

[6]We note that here we apply the original peak-to-peak amplitude F_{pp} of the *TESS* light curve rather than the standard deviation σ_{pp} used in D19.

Table 1. Model parameters of HD 21749b, HD 21749c, and the best-fitting values in the GP + transit joint fit analysis.

Parameter	Best-fitting value	Prior	Description
Planetary parameters			
P_b (d)	$35.6133^{+0.0005}_{-0.0006}$	$\mathcal{N}^a$ (35.6, 0.1^2)	Orbital period of HD 21749b
$T_{0,\,b}$ (BJD)	$2458350.3122^{+0.0007}_{-0.0007}$	$\mathcal{N}$ (2458350.3, 0.1^2)	Mid-transit time of HD 21749b
$r_{1,\,b}$	$0.7865^{+0.0310}_{-0.0340}$	$\mathcal{U}^b$ (0, 1)	Parametrization for p and b
$r_{2,\,b}$	$0.0377^{+0.0011}_{-0.0010}$	$\mathcal{U}$ (0, 1)	Parametrization for p and b
e_b	0	Fixed	Orbital eccentricity of HD 21749b
ω_b (deg)	90	Fixed	Argument of periapsis of HD 21749b
P_c (d)	$7.7902^{+0.0004}_{-0.0006}$	$\mathcal{N}$ (7.8, 0.1^2)	Orbital period of HD 21749c
$T_{0,\,c}$ (BJD)	$2458332.2783^{+0.0035}_{-0.0032}$	$\mathcal{N}$ (2458332.3, 0.1^2)	Mid-transit time of HD 21749c
$r_{1,\,c}$	$0.4780^{+0.1217}_{-0.0980}$	$\mathcal{U}$ (0, 1)	Parametrization for p and b
$r_{2,\,c}$	$0.0149^{+0.0007}_{-0.0007}$	$\mathcal{U}$ (0, 1)	Parametrization for p and b
e_c	0	Fixed	Orbital eccentricity of HD 21749c
ω_c (deg)	90	Fixed	Argument of periapsis of HD 21749c
TESS photometry parameters			
D_{TESS}	$0.868^{+0.009}_{-0.008}$	$\mathcal{N}$ (0.87, 0.01^2)	TESS photometric dilution factor
M_{TESS} (ppm)	245^{+1159}_{-1142}	$\mathcal{N}$ (0, 0.1^2)	Mean out-of-transit flux
σ_{TESS} (ppm)	166^{+1}_{-2}	$\mathcal{J}^c$ (10^{-6}, 10^6)	TESS additive photometric jitter term
q_1	$0.32^{+0.12}_{-0.09}$	$\mathcal{U}$ (0, 1)	Quadratic limb darkening coefficient
q_2	$0.66^{+0.22}_{-0.31}$	$\mathcal{U}$ (0, 1)	Quadratic limb darkening coefficient
Stellar parameters			
$\rho_\star$ (kg m^{-3})	4066^{+742}_{-690}	$\mathcal{J}$ (100, 100^2)	Stellar density
GP hyperparameters			
B_{TESS} (ppm)	$3.8^{+1.4}_{-1.3}$	$\mathcal{J}$ (10^{-6}, 100)	Covariance amplitude of GP component
C_{TESS} [10^{-6}]	$416.2^{+2152.2}_{-407.5}$	$\mathcal{J}$ (10^{-6}, 100)	Factor of GP component
L (d)	$57.8^{+23.2}_{-19.9}$	$\mathcal{J}$ (0.01, 100)	Exponential evolutionary timescale of GP component
$P_{\rm rot}$ (d)	$31.2^{+1.6}_{-0.8}$	$\mathcal{U}$ (30, 40)	Periodic timescale of GP component
Derived parameters	HD 21749b	HD 21749c	
$R_{\rm P}/R_\star$	$0.0377^{+0.0011}_{-0.0010}$	$0.0149^{+0.0008}_{-0.0007}$	Planet radius in units of stellar radii
b	$0.676^{+0.046}_{-0.051}$	$0.238^{+0.190}_{-0.149}$	Impact parameter
$a/R_\star$	$64.84^{+3.73}_{-3.89}$	$23.54^{+1.35}_{-1.41}$	Semimajor axis in units of stellar radii
i (deg)	$89.40^{+0.07}_{-0.08}$	$89.44^{+0.36}_{-0.52}$	Inclination angle
a (au)	$0.209^{+0.022}_{-0.021}$	$0.076^{+0.008}_{-0.008}$	Semimajor axis
$R_{\rm P}$ ($R_\oplus$)	$2.86^{+0.21}_{-0.20}$	$1.13^{+0.11}_{-0.10}$	Radius
$T_{\rm eq}$ (K)	407^{+22}_{-19}	676^{+36}_{-32}	Equilibrium temperature

$^a\mathcal{N}(\mu,\ \sigma^2)$ means a normal prior with mean μ and standard deviation σ.

$^b\mathcal{U}(a, b)$ stands for a uniform prior ranging from a to b.

$^c\mathcal{J}(a, b)$ stands for a Jeffrey's prior ranging from a to b.

time-scale L and periodic time-scale $P_{\rm rot}$ from the photometry-only fit into consideration and set Gaussian priors on both parameters for the RV fit accordingly. We set uninformative, wide Jeffrey's priors on the other GP parameters, similar to our transit fit (see Table 3). We do not take the $\sigma_{P_{\rm rot}} = 1.5$ d directly from the transit fit posterior but instead choose to set a relatively wide prior with $\sigma_{P_{\rm rot}} = 4$ d. This choice of a relatively wide prior is to account for any potential systematic bias in the measurement of $P_{\rm rot}$ due to the relatively short baseline of the *TESS* photometry, as well as possible changes in $P_{\rm rot}$ due to changes in spot latitudes and differential rotation (see Section 3.1). Considering that the stellar rotation period is close to the orbital period of HD 21749b, which may present additional challenges in modelling, we fix the orbital period and the time of inferior conjunction of HD 21749b based on the transit ephemeris. We compare the results from global and instrument-by-instrument GP model and find $\Delta \ln Z \sim 2$, and thus we employ the simpler global GP model with fewer degrees of freedom.

The RV residuals to the Keplerian-only model have prominent structures in the high-cadence PFSS data, suggesting strong correlated noise. After adding the GP model, such structures no longer exist. Compared with the previous Keplerian-only 1pl model, the GP + 1pl model has a significant improvement in the Bayesian model log-evidence ($\Delta \ln Z = \ln Z_{GP + 1pl} - \ln Z_{1pl} = 181$). Therefore, we consider the GP+1pl model (M2) to be favoured over the Keplerian 1pl model (M1). This best-fitting GP + 1pl model has an RV semi-amplitude K_b of 4.86 ± 0.61 m s^{-1} and an eccentricity of 0.164 ± 0.062, leading to a mass measurement of 20.0 ± 2.7 M$_\oplus$ (assuming the host star has a mass of $M_\star = 0.73 \pm 0.07$ M$_\odot$; D19). This value is a little smaller than but still consistent with the previous estimate $22.7^{+2.2}_{-1.9}$ M$_\oplus$ in D19. The best-fitting RV model and the corresponding phase-folded RV curve for HD 21749b are shown in Figs 8 and 9. Fig. 10 shows the posterior distributions of the parameters. We report all relevant $\ln Z$ of different models in Table 2 and all the best-fitting parameters and their prior settings for this
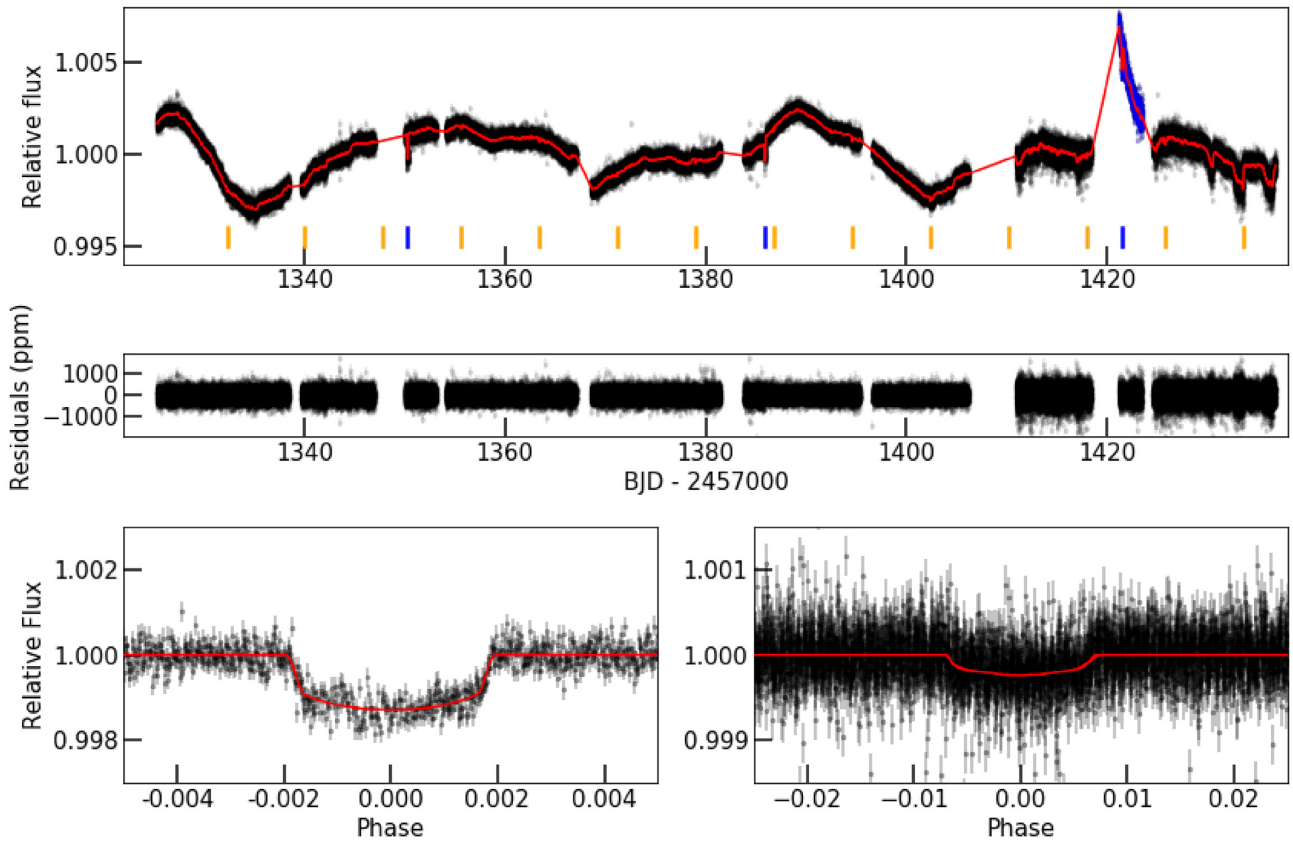
Figure 6. Top panel: The full *TESS* discovery light curve (black points) of HD 21749 along with the best-fitting GP + transit model (solid red line). Expected transits of HD 21749b and HD 21749c are marked in blue and orange ticks. The highlighted points between 1420 and 1440 have a strong downturn feature probably caused by systematics, although it did not affect the results of our GP model (see Section 3.2). Middle panel: Residuals after subtracting the best-fitting model. Bottom panels: Phase-folded light curve of HD 21749b and HD 21749c, respectively, with best-fitting GP model subtracted. The best-fitting transit models are shown as red solid lines.
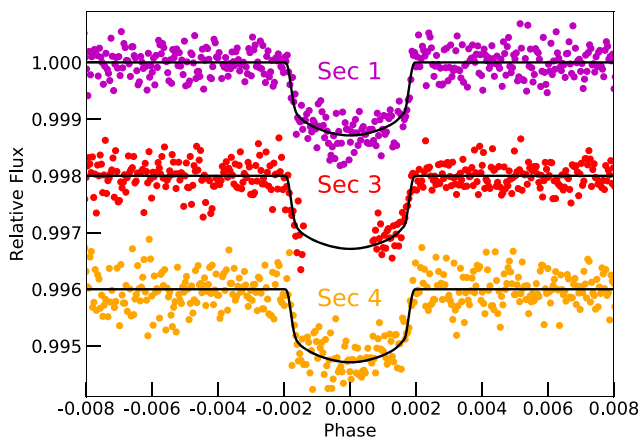
Figure 7. The phase-folded *TESS* light curves of HD 21749 from different sectors with best-fitting transit models shown as black solid lines. The best-fitting GP model has been subtracted. See Section 3.2.

GP + 1pl model in Table 3. A recent work from Kosiarek & Crossfield (2020) suggests exercising caution when using periodograms or ACF method to determine a stellar rotation period as it was not always the highest peak in these plots. Since the *TESS* photometry only covers ~3 stellar rotation cycles of HD 21749, we perform additional tests to see whether different prior settings on $P_{\rm rot}$ would have a significant

Table 2. Model comparison of RV fits with juliet.

Model	Type	$P_{\rm planet}$ prior	$\ln Z$	$\Delta \ln Z$
M1	1pl	$\mathcal{F}_b^a$ (35.613)	-792.1	180.8
M2	GP + 1pl	$\mathcal{F}_b$ (35.613)	-611.3	0
M3[b]	2pl	$\mathcal{F}_b$ (35.613) $\mathcal{J}_d$ (10^2, 10^4)	-787.6	176.3
M4	GP + 2pl	$\mathcal{F}_b$ (35.613) $\mathcal{U}_d$ (2000, 4500)	-610.3	-1.0

[a] $\mathcal{F}(\mu)$ means fixing the orbital period equal to μ.
[b] See Section 5.2 for M3 and M4.

effect on the measurement of K_b. We run two more GP + 1pl fits for all RV data with (1) a much narrower Gaussian prior on $P_{\rm rot}$ centering at 31 d with $\sigma_{P_{\rm rot}} = 1$ d; (2) a wide uniform prior between 25 and 60 d. We obtain $K_b = 4.85 \pm 0.63$ and $K_b = 4.89 \pm 0.66$ m s^{-1}, respectively, which agree with the previous value derived from the original prior setting within 1σ, indicating that K_b is not sensitive to our prior choice on $P_{\rm rot}$.

3.3.3 GP + 2pl model for all data

We then run a GP + 2pl fit to put a mass constraint on HD 21749c. We fix the orbital periods of both planets (HD 21749b and HD 21749c), set a narrow uniform prior on K_c between 0 and 3 m s^{-1} and retain the same priors on the GP hyperparameters with the GP + 1pl model. We

Table 3. Model parameters of HD 21749b and the best-fitting values in the GP + Keplerian (GP + 1pl) analysis for all RV data.

Parameter	Best-fitting value	Prior	Description
Planetary parameters			
P_b (d)	35.613	Fixed	Orbital period of HD 21749b
$T_{0,b}$ (BJD)	2458350.312	Fixed	Mid-transit time of HD 21749b
$e_b \sin \omega_b$	$0.105^{+0.082}_{-0.084}$	$\mathcal{U}(-1, 1)$	Parametrization for e and ω of HD 21749b
$e_b \cos \omega_b$	$-0.090^{+0.072}_{-0.071}$	$\mathcal{U}(-1, 1)$	Parametrization for e and ω of HD 21749b
RV parameters			
μ_{HARPSF} (m s^{-1})	$-1.18^{+0.89}_{-0.92}$	$\mathcal{U}(-10, 10)$	RV offset for pre-upgrade HARPS (HARPSF)
σ_{HARPSF} (m s^{-1})	$0.91^{+0.47}_{-0.46}$	$\mathcal{U}(0, 10)$	Jitter term for pre-upgrade HARPS (HARPSF)
μ_{HARPSS} (m s^{-1})	$-5.70^{+2.30}_{-2.10}$	$\mathcal{U}(-10, 10)$	RV offset for post-upgrade HARPS (HARPSS)
σ_{HARPSS} (m s^{-1})	$0.90^{+0.43}_{-0.42}$	$\mathcal{U}(0, 10)$	Jitter term for post-upgrade HARPS (HARPSS)
μ_{PFSF} (m s^{-1})	$0.46^{+0.87}_{-0.87}$	$\mathcal{U}(-10, 10)$	RV offset for pre-upgrade PFS (PFSF)
σ_{PFSF} (m s^{-1})	$1.58^{+0.77}_{-0.78}$	$\mathcal{U}(0, 10)$	Jitter term for pre-upgrade PFS (PFSF)
μ_{PFSS} (m s^{-1})	$0.74^{+1.13}_{-1.18}$	$\mathcal{U}(-10, 10)$	RV offset for post-upgrade PFS (PFSS)
σ_{PFSS} (m s^{-1})	$0.27^{+0.15}_{-0.15}$	$\mathcal{U}(0, 10)$	Jitter term for post-upgrade PFS (PFSS)
K_b (m s^{-1})	$4.86^{+0.61}_{-0.60}$	$\mathcal{N}(5.5^a, 2^2)$	RV semi-amplitude of HD 21749b
GP hyperparameters			
B ((m s$^{-1})^2$)	$16.923^{+3.539}_{-2.949}$	$\mathcal{J}(10^{-3}, 10^3)$	Covariance amplitude of the global GP component
C	$0.025^{+0.207}_{-0.022}$	$\mathcal{J}(10^{-3}, 10^3)$	Factor of the global GP component
L (d)	$20.049^{+7.109}_{-5.362}$	$\mathcal{N}(57.8, 50^2)$	Exponential evolutionary time-scale of the global GP component
P_{rot} (d)	$34.1^{+2.4}_{-2.7}$	$\mathcal{N}(31, 4^2)$	Periodic time-scale of the global GP component
Derived parameters	HD 21749b	HD 21749c	
e	$0.164^{+0.062}_{-0.058}$	–	Orbital eccentricity
ω (deg)	125^{+31}_{-30}	–	Argument of periapsis
M_P (M$_\oplus$)	$20.0^{+2.7}_{-2.7}$	$<3.5^b$	Mass
ρ_p (g cm^{-3})	$4.7^{+1.9}_{-1.4}$	<13.2	Density

^{a}This initial guess value 5.5 m s^{-1} is taken from D19.
^{b}This is not a statistically significant measurement but the 3σ mass upper limit.
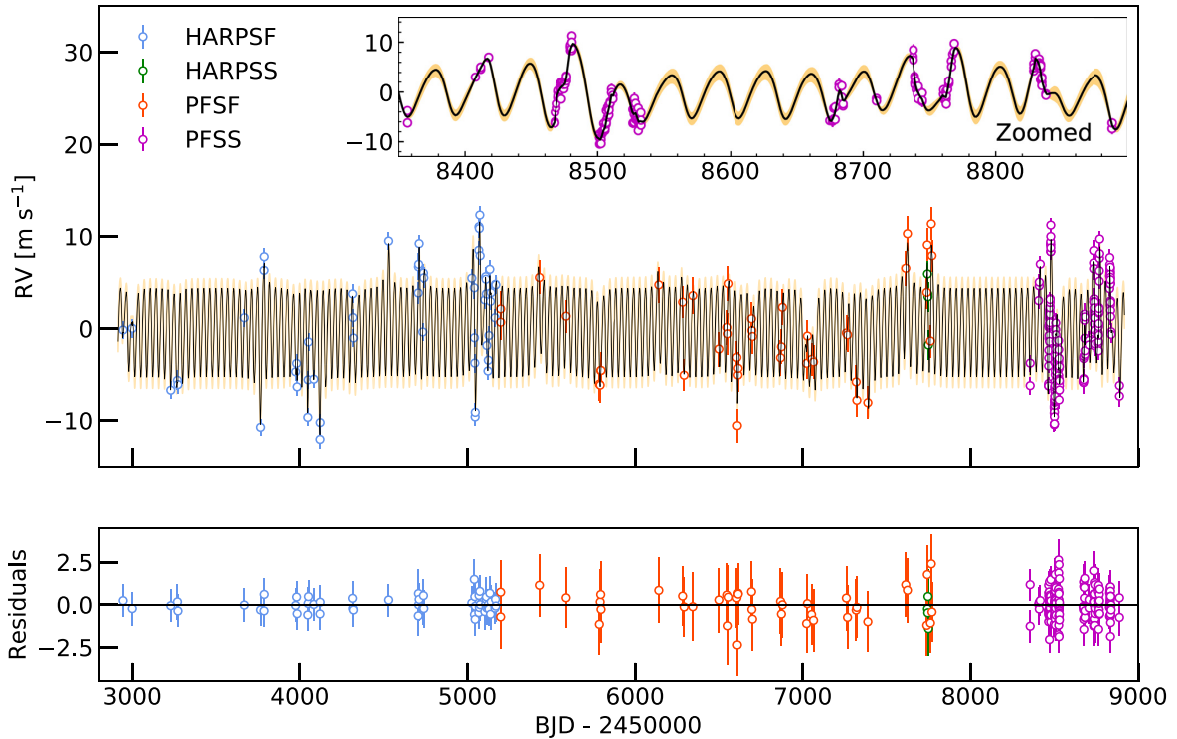
Figure 8. Top panel: Pre-upgrade HARPS (HARPSF), post-upgrade HARPS (HARPSS), pre-upgrade PFS (PFSF), and post-upgrade PFS (PFSS) radial velocity data along with the best-fitting GP + 1pl model shown as a black solid line. Zoomed-in PFSS data are shown on the top right. Bottom panels: Residuals in m s^{-1} after subtracting the best-fitting model. The error bars are the quadrature sum of the best-fitting instrument jitter term and the measurement uncertainties for all RVs.
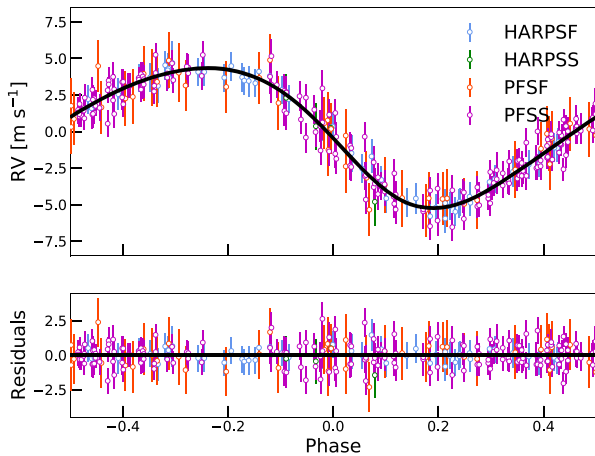
Figure 9. RVs phase-folded to the period of HD 21749b (35.613 d). The RVs plotted here are the original RVs subtracting the estimated stellar activity signals represented by the best-fitting GP model (see Section 3.3). The best-fitting Keplerian model is shown as a black solid line. The residuals in m s^{-1} are shown in the lower panel.

fit a circular orbit for HD 21749c and obtain $K_c = 0.65 \pm 0.26$ m s^{-1}, which corresponds to a 3σ mass upper limit of ~ 3.5 M$_\oplus$ estimated using the 99.7 per cent value of K in the posterior distribution.

3.3.4 GP + 1pl model for PFSS-only data

Finally, we repeat the GP + 1pl fit for the PFSS data independently because: (1) the time-scale of the stellar activity is much smaller than the total RV baseline (>6000 d); (2) only the PFSS data have a sufficiently high cadence that well samples the stellar activity signals. We obtain $P_{\rm rot} = 32.4 \pm 3.6$ d which is consistent with our findings in Sections 3.1 and 3.2. The best-fitting value of K in this case, $K_{\rm b} = 4.9 \pm 1.2$ m s^{-1}, agrees with our estimates above using the full data set within 1σ. Fig. 11 shows the total RV curve and the corresponding predicted GP model for this PFSS-only fit. The ~ 6 m s^{-1} semi-amplitude of the GP model suggests that the stellar rotation indeed has a significant contribution to the RVs. Although having similar periods, the planetary signal from HD 21749b and the best-fitting GP model for stellar activity are not always in phase, which is expected given the stochastic nature of the activity signal caused by stellar rotation. This disentanglement in phase space is essentially what enables us to tease out the stellar activity signals and obtain a more robust estimate of the planet's orbit. We list the free parameters and their priors along with the best-fitting values for this PFSS-only fit in Table A1.

We also explore modelling options other than a GP to mitigate the effects of stellar activity. Given that the activity indicator $S_{\rm HK}$ has a strong correlation with the RVs in the PFSS-only data, we first decide to perform an independent joint fit along with linear activity model. The large scatter and the clear correlated noise in the RV residuals motivate us to use a quadratic activity model instead with the form

$$RV_{\rm tot}(t_i) = \gamma + RV_{\rm Kep}(t_i) + \alpha \cdot S_{\rm HK}(t_i) + \beta \cdot S_{\rm HK}^2(t_i), \qquad (6)$$

where γ is the RV zero-point. $RV_{\rm Kep}$ represents the Keplerian signal while α, β are the coefficients of the activity model. We apply the same RV prior settings as the ones that used in the previous GP + 1pl fit for PFSS data. A Markov chain Monte Carlo (MCMC) analysis is carried out to explore the posterior probability distribution of the orbital parameters with EMCEE (Foreman-Mackey et al. 2013). We

initialize 250 walkers and run for 20 000 steps with the first 5000 steps abandoned as burnt-in sample. However, we do not find a clear improvement of the final result, which indicates that the current simple polynomial activity model cannot successfully characterize the stellar rotation signal.

4 STELLAR ACTIVITY SIMULATION

As mentioned in Section 3.3, the RV variation caused by the planet perturbation is at the same level as the stellar activity effect and the orbital period is similar to the rotation time-scale. Such extreme entanglement calls for extra caution when determining how stellar activity affects our estimate of the Keplerian signal. With all of the above in mind, we perform simulations to evaluate the robustness of our GP + Keplerian model that disentangles these two different signals.

We choose to perform the simulations in the context of the PFSS-only fit because of its high cadence sampling. We first create 10 000 sets of RV data from our best-fitting GP models using CELERITE based on the median GP hyperparameters values taken from the posterior distribution of our PFSS-only GP + 1pl fit. After the superposition of a simulated Keplerian component representing HD 21749b with K at 4.9 m s^{-1},[7] and a random Gaussian white noise according to our best-fitting RV jitter, we apply the GP + 1pl fitting algorithm to these artificial data and minimize the likelihood function using the least-squares method. For comparison, we repeat this with the Keplerian-only 1pl fit. The upper panel of Fig. 12 shows the distribution of ΔK, defined as the difference between the fitted K and the input $K = 4.9$ m s^{-1} in the simulation. For most cases of the GP + 1pl model, we obtain $|\Delta K| \lesssim 1$ m s^{-1} with a standard deviation of ~ 1.0 m s^{-1}. The evenly distributed ΔK near zero suggests that the GP + 1pl model does not bias the real planet signal in our case. Without a GP model, we do not find a significant biased K estimate but we do arrive at a slightly broader distribution with a standard deviation around 1.8 m s^{-1}, indicating a lower precision than the GP + 1pl model.

We then generate another 10 000 sets of correlated noise regarded as stellar activity signals based on the GEORGE package with a Matern32 kernel (Foreman-Mackey 2015)

$$k_{i,j}(\tau) = A^2 \left(1 + \sqrt{3\frac{\tau^2}{\lambda^2}}\right) \exp\left(-\sqrt{3\frac{\tau^2}{\lambda^2}}\right), \qquad (7)$$

where τ is the time-lag, A is the covariance amplitude, and λ is the correlation time-scale. We fix λ equal to the median value in the posterior distribution of L from our PFSS-only GP + 1pl fit as both λ and L contribute to the exponential term of two GP kernels. We randomly select several hyperparameter A between 1 and 10, and examine the amplitude of the resulting signals. For convenience, we finally fix A equal to 4, making the expected RV variation caused by the stellar activity close to the level we saw in the PFSS data (Fig. 11). Similarly, we add the same simulated Keplerian component and a random Gaussian white noise as mentioned above, and repeat the 1pl and GP + 1pl fit. The corresponding ΔK distribution is shown in the lower panel of Fig. 12. By utilizing a different GP kernel to generate stellar activity signals, we notice that the standard deviation of ΔK derived from the 1pl fit has a small decrease but it is still much larger than the typical reported error bar (~ 0.5 m s^{-1}). Simultaneously, we obtain similar standard deviations of the ΔK distribution in the GP + 1pl fit case, which are also consistent with the reported error

---

[7]This value of K is taken from the GP+1pl fit for PFSS data, which is consistent with what we find in the GP + 1pl fit for all RV data.
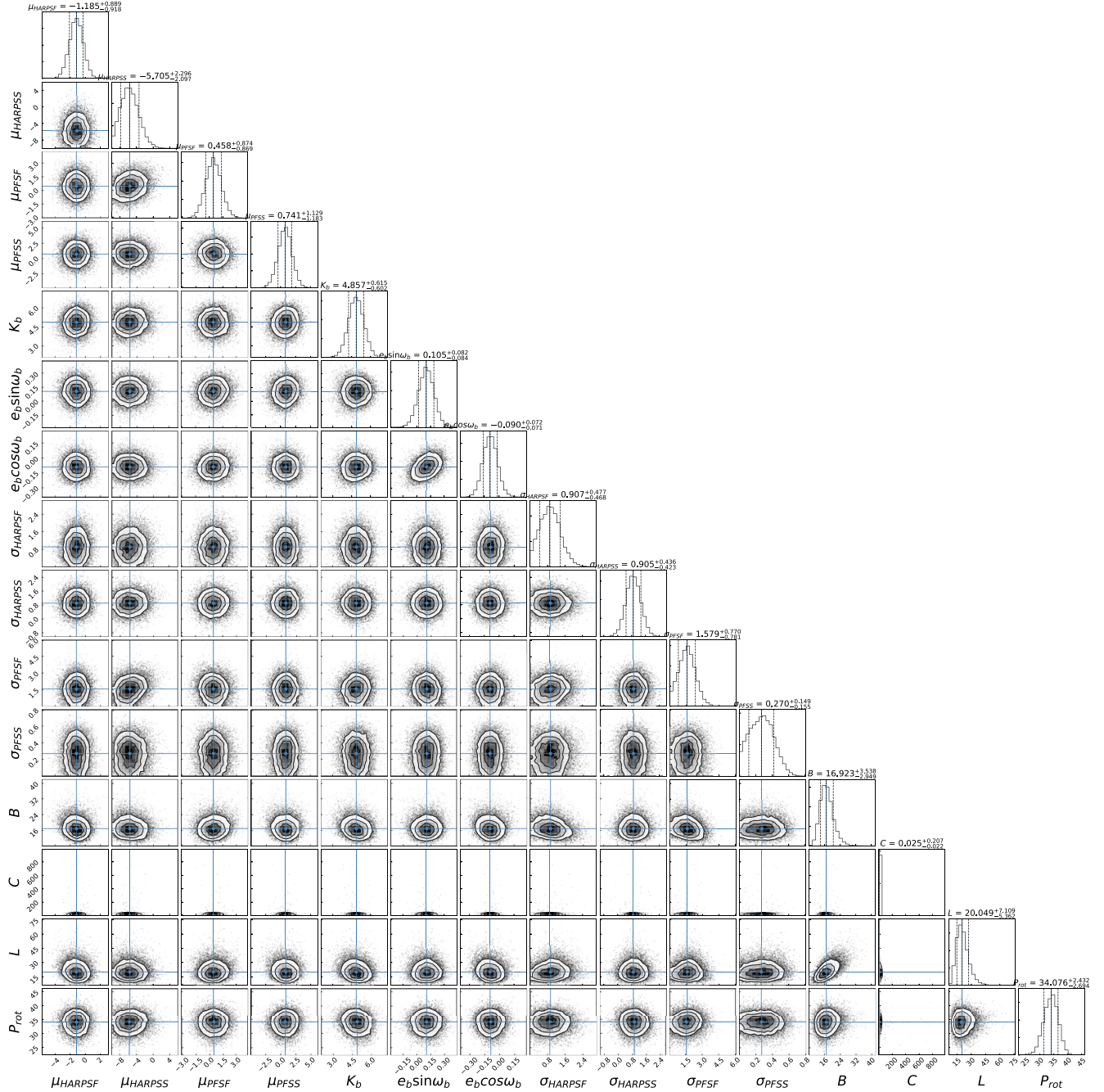
Figure 10. Posterior distributions of the parameters from the fit with the GP + 1pl model using all RV data.
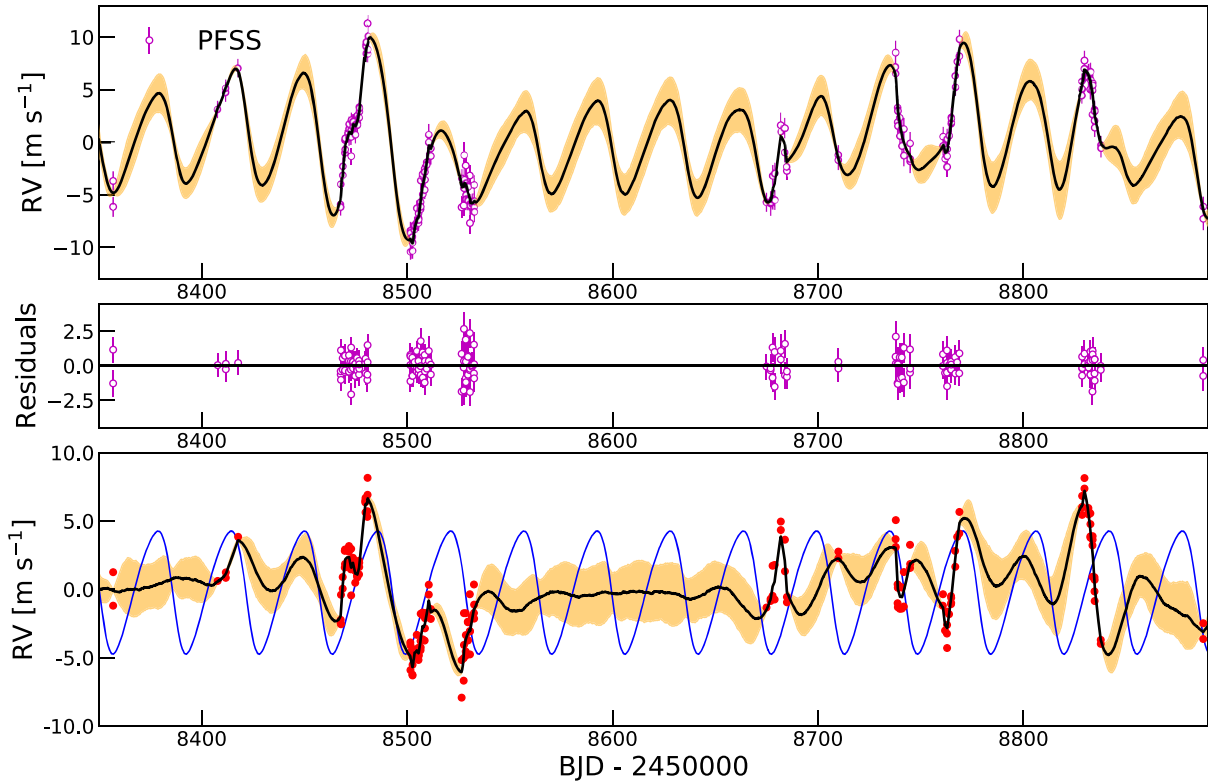
bar ($\sim 1 \, \mathrm{m\,s^{-1}}$). We show the injected GP models of 5 simulated RV data sets in Fig. 13.

Furthermore, we run 15 additional independent fits[8] with nested sampling for both GP + 1pl and 1pl model to compare their accuracy and precision. The results are shown in Fig. 14. Although the 1pl fit appears to give a more precise measurement of K implied by a narrower posterior distribution with a typical error bar of $\sim 0.5 \, \mathrm{m\,s^{-1}}$, the large deviation and scatter of the best-fitting K values from the input true value of $K\,(4.9 \, \mathrm{m\,s^{-1}})$ suggest unaccounted uncertainties in

the modelling, which could lead to a biased estimate of the RV semi-amplitude with an underestimated error bar. Instead, in the GP + 1pl fit, we find the estimated K values are more often closer to the true value. In addition, the amount of scatter in ΔK is consistent with the reported scatter in the posterior distribution of K, at about $1 \, \mathrm{m\,s^{-1}}$. The result of these simulations suggest that the Keplerian-only model often reports an underestimated error bar for K, and it is also subject to more uncertainties when measuring K than the model with stellar activity taken into account.

As a final test for the robustness of our model, we check the detection efficiency of our methodology. We fix the stellar rotation signal to our best-fitting GP model to the real PFSS data and generate a total of 10 planet signals with various K ranging from 1 to

---

[8]We only run 15 simulations with nested sampling, because each run is relatively computational intensive.

Figure 11. Top panel: PFSS data along with the best-fitting GP + 1pl model. The shaded yellow region represents the 1σ estimate. Middle panel: RV residuals after subtracting the best-fitting model. Bottom panel: The red points are the total RV subtracting the best-fitting Keplerian component of the GP + 1pl fit for PFSS-only data. The black line is the predicted GP curve with a semi-amplitude ~ 6 m s^{-1}. The best-fitting Keplerian orbit is shown as the blue curve.

10 m s^{-1}. Similarly, we add these two parts together along with a random Gaussian white noise for each sample. We perform the same GP + 1pl fit for the artificial RV data with nested sampling.[9] We present the final result in Fig. 15, which suggests that the detection limit of our methodology is 2–4 m s^{-1} as the size of the error bar makes the 3σ detection near 4 m s^{-1}. This detection limit is a lower level than the ~ 4.9 m s^{-1} variation we found in the real RV data, validating the robustness of our measurement. We note that this added activity + white noise component is very similar to adding the residuals of the original RVs subtracting the best-fitting Keplerian model, given that our GP model had a high goodness of fit to the activity component. The difference versus using the residuals is that we use a different set of additional Gaussian noise in each simulation at a different K value, randomizing the white noise component.

5 DISCUSSIONS

5.1 HD 21749b as an atmospheric characterization target

Warm sub-Neptunes or super-Earths around nearby bright stars are extremely rare. According to data from the NASA Exoplanet Archive, among over 3000 confirmed exoplanets smaller than Neptune, only 27 are around stars with 2MASS K_s band magnitude brighter than 10 mag. If we limit the equilibrium temperature of the planet to be lower than 500 K, then there are only 6 such planets, all around M dwarfs except for HD 21749b. HD 21749b also has the brightest host star in the K_s band (5.4 mag) and by far the brightest in the optical V band (8.1 mag), making it an attracting object for future atmospheric characterization.

Having an accurate and precise measurement for the planetary mass is very important for reliably retrieving the atmospheric parameters, as demonstrated by the work of Batalha et al. (2019). Our updated measurements for HD 21749b in this work provide the latest robust estimates for the density and surface gravity for this favourable target for atmospheric characterization. D19 reported HD 21749b as the second densest sub-Neptune with a density of $7.6^{+1.6}_{-1.3}$ g cm^{-3}, after K2-66b (Sinukoff et al. 2017). However, we obtain a smaller mean density, $4.80^{+1.98}_{-1.40}$ g cm^{-3}, combining our updated mass and radius estimates of HD 21749b. The estimated surface gravity of HD 21749b also decreased by ~ 20 per cent with the updated mass and radius estimates. As shown in the mass–radius diagram (Fig. 16), HD 21749b is consistent with a rocky composition of magnesium silicate and water. We simply evaluate the radius of the rock core $R_{core} = 2.1 \pm 0.1$ R$_\oplus$ according to equation (1) in Lopez & Fortney (2014), which implies that HD 21749b could hold a relatively thick gaseous envelope.

HD 21749 is a suitable source for ground-based atmosphere characterization given its brightness. However, it is not an ideal target for *JWST*. First, as noted by D19, HD 21749b does not have a very high Transmission Spectroscopic Metric[10] (TSM; Kempton et al. 2018). Moreover, with a $J \sim 6$ mag, HD 21749 sits on, or

---

[9]Note that we expand the prior bound on K with a slightly larger $\sigma_K = 5$ m s^{-1}.

[10]With the updated planetary parameters, we obtain TSM = 75^{+46}_{-29} for HD 21749b.
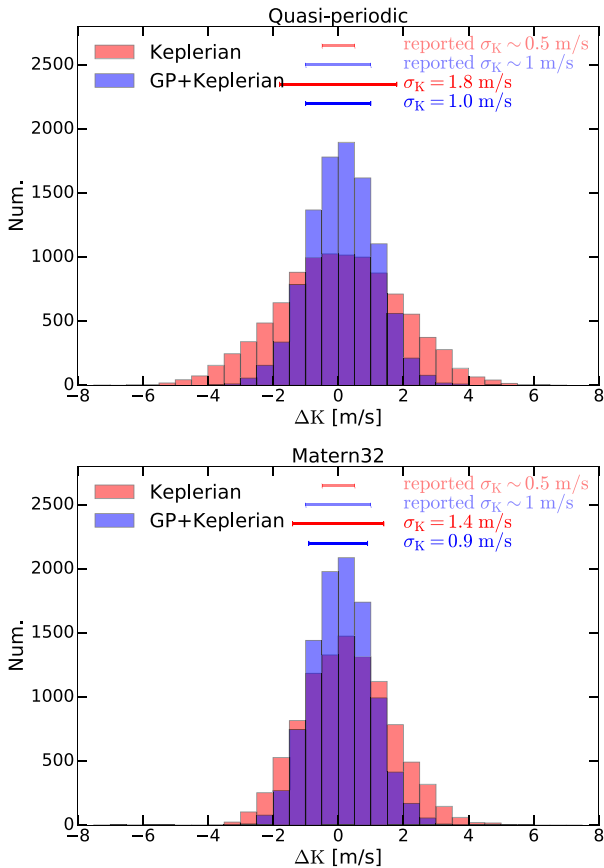
Figure 12. *K* difference distribution of 10 000 simulated RV data derived from the 1pl and GP + 1pl fit using the least-squares minimization method. Different panels show the results with stellar activity signals generated by different GP kernels (see Section 4). The standard deviations of two Δ*K* distributions are shown as horizontal ticks above the histograms while the typical reported error bars from each kind of fit are the translucent ones (see Fig. 14). The corresponding values are on the upper right.

surpasses the edge of hard saturation for two of the Bright Object Time Series (BOTS) instruments of *JWST*.

A *JWST* integration is composed of a reset of the detector, followed by a sequence of non-destructively sampled *groups*. The time it takes to read out one group, and reset the detector, is specified by each observing mode's unique frame time, t_f. Currently, the Astronomer's Proposal Tool[11] requires that each BOTS mode has at least two groups per integration. Therefore, the 'hard' saturation limit of each instrument is defined by whether the electron count of any pixel on the subarray has surpassed the full well limit at the end of two groups (Pontoppidan et al. 2016; Batalha et al. 2017). For NIRISS SOSS's smallest subarray (SUBSTRIP96, $t_f = 2.2$ s), assuming an optimistic saturation limit of 100 per cent full well, there would be 14 028 pixels saturated at the end of the first group. For NIRSpec G395H ($t_f = 0.90$ s), there would be 1265 pixels saturated at the end of the first group. Given that G395H is NIRSpec's highest resolution and longest wavelength spectrograph, it would preclude observations from other NIRSpec BOTS modes (i.e. Prism, G140M/H, G235M/H, or G395M). Thus, even if the 2 group minimum requirement is decreased to 1 group, NIRISS and NIRspec observations would be unattainable.

On the other hand, both NIRCam and MIRI would be free of saturation concerns. Using NIRCam's 4amp readout mode ($t_f = 0.34$ s), an *F322W2* observation could be made with 3 groups without surpassing the optimistic 100 per cent full well saturation limit. An observation with an integration time of $2T_{14}$, would result in a minimum precision of 67 ppm at 2.8 μm where *F322W2*'s native resolution is $R = 1397$ (or roughly 20 ppm if binned to $R = 100$). Likewise, MIRI LRS ($t_f = 0.159$ s) could also fit a 3 group observation assuming 100 per cent full well. Similarly, an observation with an integration time of $2T_{14}$ would result in a minimum precision of 23 ppm for MIRI LRS at its native resolution of $R = 100$. These estimates could be lower limits if faster readout patterns are approved in Cycle 2 (see fig. 2 in Batalha et al. 2018). Because of the reset-read pattern, integrations with three groups have an efficiency (duty cycle) of just $(n - 1)/(n + 1) = 50$ per cent. The most efficient of these patterns has the potential of yielding near ~ 100 per cent efficiency for bright targets. Additionally, the NIRCam DHS mode is also being considered for Cycle 2 + (Schlawin et al. 2017). If approved, this would enable short wavelength ($1 \sim 2$ μm) $R = 300$ spectroscopy on up to $K \sim 4.52$ targets.

5.2 Additional planets in the HD 21749 system?

To search for additional potential non-transiting planets in the HD 21749 system, we first perform an independent 2pl fit (M3; as listed in Table 2). We place a wide log-uniform prior on the period *P* between 10 and 10^4 d along with a wide uniform prior on the RV semi-amplitude *K*. We find a convergence in the $P - K$ space, implying a possible outer planet companion with period around 3500 d. This periodic signal shows up as a weak peak in the GLS periodogram of the total RV data (see Section 2.3). This 2pl model has a slight increase ln *Z* ($\Delta \ln Z = \ln Z_{2pl} - \ln Z_{1pl} = 4.5$). Building on the results from the 2pl model, we perform a further GP + 2pl fit (M4) which allows *P* to vary uniformly between 2000 and 4500 d. We measure $K = 2.53 \pm 0.91$ m s^{-1} for this hypothetical planet. With $P = 3279^{+352}_{-307}$ d, if this signal were indeed caused by a real planet companion, it would correspond to a sub-Saturn planet at $3.9^{+0.3}_{-0.3}$ au with $M_p \sin i = 0.5^{+0.2}_{-0.2} M_{Sat}$. However, the increase in the Bayesian evidence from the GP + 1pl model, $\ln Z_{GP + 2pl} - \ln Z_{GP + 1pl}$, is only about 1.0, and thus we conclude that there is insufficient evidence for such a planet in the current RV data.

Such a conclusion is perhaps not surprising, given that the HARPS and PFS data do not have any significant overlap in time over the 20-yr baseline that they span, and the proposed planet's period is around 10 yr. In addition, it would be extremely challenging to mitigate the stellar activity signals arising from an ~30 d stellar rotation with an amplitude around 5 m s^{-1} over the course of decades to detect a planet with a considerably smaller RV semi-amplitude ($K \sim 2.5$ m s^{-1}). To make things worse, we cannot rule out that the ~3500 d signal is from the long-term magnetic cycles of the host star, similar to the 11-yr solar magnetic cycle. None the less, given the 3σ constraint on *K* and *P* above and the time baseline of our RV data, we have ruled out the existence of an outer gas giant planet with mass down to Saturn mass and period up to roughly 10 yr. Future RV follow-up observations with high precision and high cadence could measure the mass of HD 21749c and might be able to reveal additional planets in the system.

6 SUMMARY AND CONCLUSIONS

In this paper, we characterize the HD 21749 planetary system using the publicly available *TESS*, HARPS, and PFS data in D19 combined with an additional set of more recent PFS RVs. We apply GP models
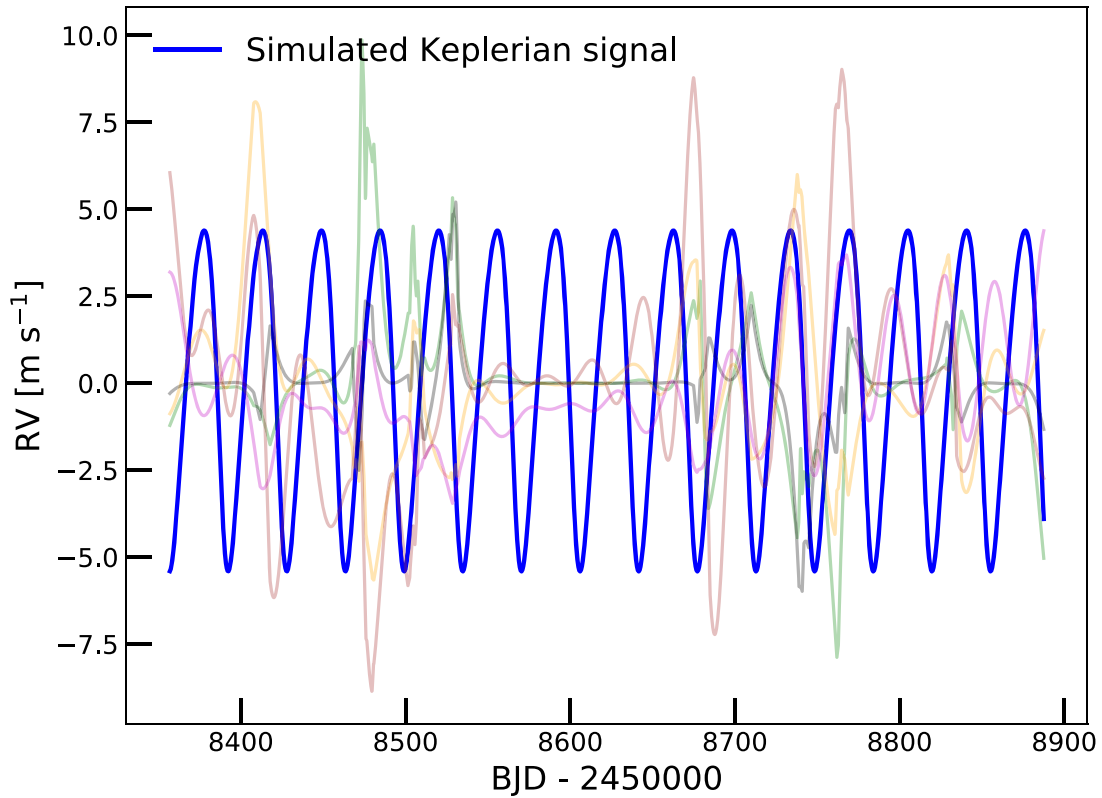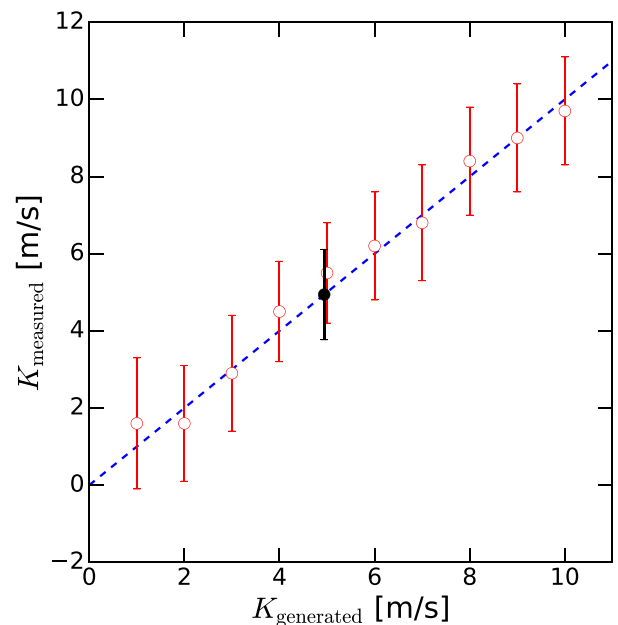
Figure 13. Several examples of the injected GP models representing stellar activity signals from our simulations (various light coloured curves) in comparison with the simulated planetary signal (the solid blue curve). See Section 4 for more detail.
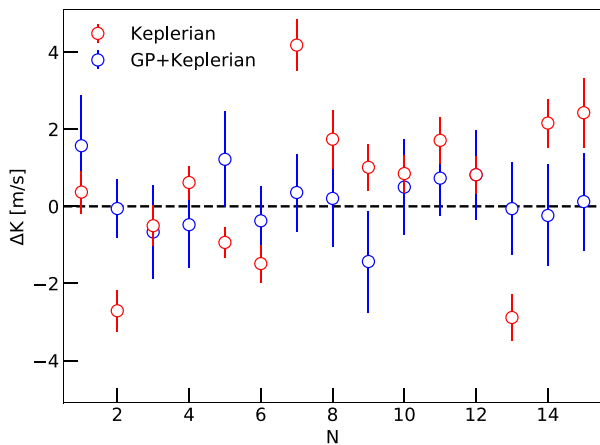

Figure 14. Difference in K between the best-fitting and the input true value from the 15 independent simulated RV data sets for both GP + 1pl and 1pl models. The 1σ errors are derived from nested sampling. The large deviation and scatter of the results from the Keplerian-only model suggest that it is more uncertain and subject to an underestimation of error bars when measuring K.

Figure 15. The generated K versus measured K using GP + 1pl model fit. The 1σ errors are derived from nested sampling. The black point represents our best-fitting K to the real PFSS data. The detection limit of our methodology is 2–4 m s^{-1}, considering the 3σ detection. See Section 4 for more detail.

in our transit and RV fits to reduce the effect of stellar rotation and improve the accuracy of the mass determination of HD 21749b. The sub-Neptune HD 21749b has a radius of $2.86 \pm 0.20\,R_\oplus$ and an orbital period of 35.6133 ± 0.0005 d. Our GP + Keplerian fit to the RV data reveals that HD 21749b has a mass of $20.0 \pm 2.7\,M_\oplus$, which agrees with the estimates in D19 within 1σ. For HD 21749c, an Earth-sized planet on a 7.79 d orbit, we constrain its radius to be $1.13 \pm 0.10\,R_\oplus$ and its mass to have a 3σ upper limit at $3.5\,M_\oplus$. Compared with D19: (1) we obtain a slightly larger planet radius for

both HD 21749b and HD 21749c as we apply an updated value of the dilution factor for the *TESS* photometry; and (2) we find a smaller RV semi-amplitude for HD 21749b after taking the stellar activity into consideration.
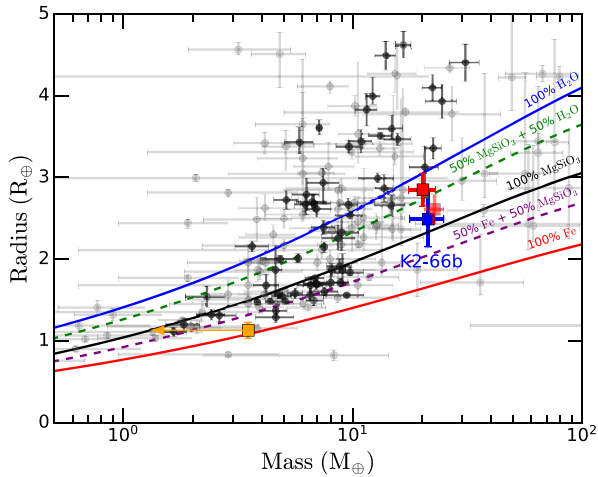
Figure 16. Mass–radius diagram in Earth units. The updated position of HD 21749b is marked as a red square while the original position is shown as the translucent one based on D19. HD 21749c is shown as an orange square (3σ mass upper limit). Black dots represent planets with precise measurement for mass and radius (uncertainty smaller than 20 per cent of the measured parameters) while grey points are planets with weak constraint on their radius or mass (data from NASA Exoplanet Archive; Akeson et al. 2013). The coloured lines are taken from theoretical models for different planetary compositions in Zeng & Sasselov (2013).

Using Monte Carlo simulations, we verify that our incorporation of a GP model in the RV data analysis does not bias the mass measurement of HD 21749b. On the other hand, our simulations reveal that a simple Keplerian fit without mitigating stellar activity signals is more likely to result in a biased measurement with an underestimated error bar for HD 21749b's RV semi-amplitude. Thus, we encourage communities to use the updated values in the future as the results in this work are more robust.

The story of HD 21749b represents a relatively challenging case for RV characterization in several ways. First, it has the inconvenient entanglement of the planetary signal and the stellar activity, which have very similar time-scales and exhibit similar RV amplitudes. Additionally, both the stellar rotation and the planet's orbital period are a bit longer than the lunar cycle, which makes it difficult to sample the rotation phase and the orbital phase continuously in complete cycles given that RV spectroscopic observations are normally scheduled during bright time. The fact that we can successfully retrieve the planet's RV semi-amplitude without significant bias illustrates the importance of nightly, high-cadence observations and proper modelling of stellar activity for such systems (similar to López-Morales et al. 2016).

ACKNOWLEDGEMENTS

DATA AVAILABILITY

This paper includes photometric data collected by the *TESS* mission, which is publicly available from the Mikulski Archive for Space Telescopes (MAST) at the Space Telescope Science Institure (STScI). The *TESS* light curve used in this work is available in ExoFOP, at https://exofop.ipac.caltech.edu/tess/target.php?id = 279741379. All spectroscopy data underlying this article are listed in the appendix.

REFERENCES

Akeson R. L. et al., 2013, PASP, 125, 989
Baglin A., Auvergne M., Barge P., Deleuil M., Catala C., Michel E., Weiss W., COROT Team, 2006, 36th COSPAR Scientific Assembly, 36, 3749
Bakos G., Noyes R. W., Kovács G., Stanek K. Z., Sasselov D. D., Domsa I., 2004, PASP, 116, 266
Barnes S. A., 2007, ApJ, 669, 1167
Batalha N. E. et al., 2017, PASP, 129, 064501
Batalha N. E., Lewis N. K., Line M. R., Valenti J., Stevenson K., 2018, ApJ, 856, L34
Batalha N. E., Lewis T., Fortney J. J., Batalha N. M., Kempton E., Lewis N. K., Line M. R., 2019, ApJ, 885, L25
Borucki W. J. et al., 2010, Science, 327, 977
Butler R. P., Marcy G. W., Williams E., McCarthy C., Dosanjh P., Vogt S. S., 1996, PASP, 108, 500
Butler R. P., Jones H. R. A., Feng F., Tuomi M., Anglada-Escudé G., Keiser S., 2019, AJ, 158, 251

Canto Martins B. L. et al., 2020, ApJS, 250, 20

Charbonneau D., Brown T. M., Latham D. W., Mayor M., 2000, ApJ, 529, L45

Chen J., Kipping D., 2017, ApJ, 834, 17

Collier Cameron A. et al., 2007, MNRAS, 375, 951

Crane J. D., Shectman S. A., Butler R. P., 2006, Society of Photo-Optical Instrumentation Engineers (SPIE) Conference Series, 6269, 626931

Crane J. D., Shectman S. A., Butler R. P., Thompson I. B., Burley G. S., 2008, Society of Photo-Optical Instrumentation Engineers (SPIE) Conference Series, 7014, 701479

Crane J. D., Shectman S. A., Butler R. P., Thompson I. B., Birk C., Jones P., Burley G. S., 2010, Society of Photo-Optical Instrumentation Engineers (SPIE) Conference Series, 7735, 773553

Curtis J. L., Agüeros M. A., Douglas S. T., Meibom S., 2019, ApJ, 879, 49

Dai F. et al., 2017, AJ, 154, 226

de Zeeuw T., Tamai R., Liske J., 2014, The Messenger, 158, 3

Dragomir D. et al., 2019, ApJ, 875, L7

Dumusque X., Udry S., Lovis C., Santos N. C., Monteiro M. J. P. F. G., 2011, A&A, 525, A140

Duncan D. K. et al., 1991, ApJS, 76, 383

Espinoza N., 2018, Res. Notes Am. Astron. Soc., 2, 209

Espinoza N., Kossakowski D., Brahm R., 2019, MNRAS, 490, 2262

Feng F. et al., 2019a, ApJS, 242, 25

Feng F., Lisogorskyi M., Jones H. R. A., Kopeikin S. M., Butler R. P., Anglada-Escudé G., Boss A. P., 2019b, ApJS, 244, 39

Foreman-Mackey D., 2015, Astrophysics Source Code Library, record ascl:1511.015

Foreman-Mackey D., Hogg D. W., Lang D., Goodman J., 2013, PASP, 125, 306

Foreman-Mackey D., Agol E., Ambikasaran S., Angus R., 2017, AJ, 154, 220

Fulton B. J. et al., 2017, AJ, 154, 109

Fulton B. J., Petigura E. A., Blunt S., Sinukoff E., 2018, PASP, 130, 044504

Gaia Collaboration, 2018, A&A, 616, A10

Gan T. et al., 2020, AJ, 159, 160

Gardner J. P. et al., 2006, Space Sci. Rev., 123, 485

Gilmozzi R., Spyromilio J., 2007, The Messenger, 127, 11

Gomes da Silva J., Santos N. C., Bonfils X., Delfosse X., Forveille T., Udry S., 2011, A&A, 534, A30

Grunblatt S. K., Howard A. W., Haywood R. D., 2015, ApJ, 808, 127

Haywood R. D. et al., 2014, MNRAS, 443, 2517

Henry G. W., Marcy G. W., Butler R. P., Vogt S. S., 2000, ApJ, 529, L41

Higson E., Handley W., Hobson M., Lasenby A., 2019, Stat. Comput., 29, 891

Howard A. W. et al., 2013, Nature, 503, 381

Howell S. B. et al., 2014, PASP, 126, 398

Huang C. X. et al., 2018, preprint (arXiv:1807.11129)

Jenkins J. M. et al., 2016, in Chiozzi G., Guzman J. C., eds, Proc. SPIE Conf. Ser. Vol. 9913, Software and Cyberinfrastructure for Astronomy IV. SPIE, Bellingham, p. 99133E

Jenkins J. M., 2002, ApJ, 575, 493

Jenkins J. M., Tenenbaum P., Seader S., Burke C. J., McCauliff S. D., Smith J. C., Twicken J. D., Chandrasekaran H., 2017, in Jenkins J. M., ed, Kepler Data Processing Handbook: Transiting Planet Search, Kepler Science Document, KSCI-19081-002

Kempton E. M. R. et al., 2018, PASP, 130, 114401

Kipping D. M., 2013, MNRAS, 435, 2152

Kosiarek M. R., Crossfield I. J. M., 2020, AJ, 159, 271

Kovács G., Zucker S., Mazeh T., 2002, A&A, 391, 369

Kreidberg L., 2015, PASP, 127, 1161

Law N. M. et al., 2015, PASP, 127, 234

Lomb N. R., 1976, Ap&SS, 39, 447

Lopez E. D., Fortney J. J., 2014, ApJ, 792, 1

López-Morales M. et al., 2016, AJ, 152, 204

Luque R. et al., 2019, A&A, 628, A39

Mamajek E. E., Hillenbrand L. A., 2008, ApJ, 687, 1264

Mayor M. et al., 2003, The Messenger, 114, 20

McQuillan A., Aigrain S., Mazeh T., 2013, MNRAS, 432, 1203

McQuillan A., Mazeh T., Aigrain S., 2014, ApJS, 211, 24

Oelkers R. J. et al., 2018, AJ, 155, 39

Otegi J. F., Dorn C., Helled R., Bouchy F., Haldemann J., Alibert Y., 2020, preprint (arXiv:2006.12353)

Penev K. et al., 2013, AJ, 145, 5

Pepe F. et al., 2013, Nature, 503, 377

Pepper J. et al., 2007, PASP, 119, 923

Pepper J., Kuhn R. B., Siverd R., James D., Stassun K., 2012, PASP, 124, 230

Pollacco D. L. et al., 2006, PASP, 118, 1407

Pontoppidan K. M. et al., 2016, in Alison B. P., Robert L., Chris R., Benn A. B., Seaman R. L., Benn C. R., eds, Proc. SPIE Conf. Ser. Vol. 9910, Observatory Operations: Strategies, Processes, and Systems VI. SPIE, Bellingham, p. 991016

Queloz D. et al., 2009, A&A, 506, 303

Rajpaul V., Aigrain S., Osborne M. A., Reece S., Roberts S., 2015, MNRAS, 452, 2269

Ratzloff J. K., Law N. M., Fors O., Corbett H. T., Howard W. S., del Ser D., Haislip J., 2019, PASP, 131, 075001

Ricker G. R. et al., 2014, in Oschmann J. M., Jr., Clampin M., Fazio G. G., MacEwen H. A., eds, Proc. SPIE Conf. Ser. Vol. 9143, Space Telescopes and Instrumentation 2014: Optical, Infrared, and Millimeter Wave. SPIE, Bellingham, p. 914320

Ricker G. R. et al., 2015, J. Astron. Telesc. Instrum. Syst., 1, 014003

Rogers L. A., 2015, ApJ, 801, 41

Scargle J. D., 1982, ApJ, 263, 835

Schlawin E. et al., 2017, PASP, 129, 015001

Seager S., Sasselov D. D., 2000, ApJ, 537, 916

Seager S., Deming D., Valenti J. A., 2009, Astrophys. Space Sci. Proc., 10, 123

Sinukoff E. et al., 2017, AJ, 153, 271

Speagle J. S., 2020, MNRAS, 493, 3132

Stassun K. G. et al., 2018, AJ, 156, 102

Stassun K. G. et al., 2019, AJ, 158, 138

Sullivan P. W. et al., 2015, ApJ, 809, 77

Teske J. K., Shectman S. A., Vogt S. S., Díaz M., Butler R. P., Crane J. D., Thompson I. B., Arriagada P., 2016, AJ, 152, 167

Trifonov T., Rybizki J., Kürster M., 2019, A&A, 622, L7

Trifonov T., Tal-Or L., Zechmeister M., Kaminski A., Zucker S., Mazeh T., 2020, A&A, 636, A74

Trotta R., 2008, Contemp. Phys., 49, 71

Vanderburg A. et al., 2019, ApJ, 881, L19

Vanderburg A., Plavchan P., Johnson J. A., Ciardi D. R., Swift J., Kane S. R., 2016, MNRAS, 459, 3565

Zechmeister M. et al., 2018, A&A, 609, A12

Zechmeister M., Kürster M., 2009, A&A, 496, 577

Zeng L., Sasselov D., 2013, PASP, 125, 227

APPENDIX A: GP + KEPLERIAN (GP + 1PL) ANALYSIS FOR PFSS-ONLY DATA

Table A1. Model parameters of HD 21749b and the best-fitting values in the GP + Keplerian (GP + 1pl) analysis for PFSS-only data.

Parameter	Best-fitting value	Prior	Description
Planetary parameters			
P_b (d)	35.613	Fixed	Orbital period of HD 21749b
$T_{0,b}$ (BJD)	2458350.312	Fixed	Mid-transit time of HD 21749b
$e_b \sin \omega_b$	$0.108^{+0.131}_{-0.156}$	$\mathcal{U}(-1, 1)$	Parametrization for e and ω of HD 21749b
$e_b \cos \omega_b$	$-0.064^{+0.196}_{-0.187}$	$\mathcal{U}(-1, 1)$	Parametrization for e and ω of HD 21749b
RV parameters			
μ_{PFSS} (m s^{-1})	$0.66^{+1.51}_{-1.53}$	$\mathcal{U}(-10, 10)$	RV offset for post-upgrade PFS (PFSS)
σ_{PFSS} (m s^{-1})	$0.28^{+0.17}_{-0.16}$	$\mathcal{U}(0, 10)$	Jitter term for post-upgrade PFS (PFSS)
K_b (m s^{-1})	$4.94^{+1.18}_{-1.17}$	$\mathcal{N}(5.5, 2^2)$	RV semi-amplitude of HD 21749 b
GP hyperparameters			
B ((m s^{-1})^2)	$19.442^{+7.627}_{-4.964}$	$\mathcal{J}(10^{-3}, 10^3)$	Covariance amplitude of the global GP component
C	$0.037^{+0.478}_{-0.033}$	$\mathcal{J}(10^{-3}, 10^3)$	Factor of the global GP component
L (d)	$27.693^{+10.563}_{-5.271}$	$\mathcal{N}(57.8, 50^2)$	Exponential evolutionary timescale of the global GP component
P_{rot} (d)	$32.4^{+4.1}_{-3.6}$	$\mathcal{N}(31, 4^2)$	Periodic timescale of the global GP component

APPENDIX B: ALL RVS AND STELLAR ACTIVITY INDICATORS OF HARPS AND PFS

Table B1. HARPS RVs and stellar activity indicators.

Time (BJD)	RV (m s^{-1})	RVerr (m s^{-1})	CRX	CRXerr	DLW	DLWerr
2452944.721	− 1.34	0.31	− 8.81	4.79	− 3.68	1.31
2452999.632	− 1.16	0.43	− 7.72	5.31	− 23.34	1.44
2453229.926	− 7.89	0.32	− 1.85	3.03	− 14.83	1.11
2453269.827	− 6.83	0.56	8.24	4.45	− 2.86	1.59
2453272.829	− 7.28	0.33	7.95	3.16	− 17.44	1.22
2453668.802	− 0.01	0.39	3.61	3.72	− 22.05	1.10
2453765.524	− 11.93	0.23	10.00	3.03	− 30.58	1.43
2453786.575	5.13	0.32	3.72	3.59	− 22.65	1.23
2453787.561	6.61	0.31	4.64	3.09	− 21.81	1.20
2453974.883	− 5.89	0.39	− 3.97	3.62	− 10.69	0.91
2453980.853	− 4.98	0.33	1.07	3.70	− 10.63	1.08
2453983.878	− 7.53	0.26	1.32	2.86	− 18.41	1.00
2454047.702	− 10.84	0.31	11.24	3.36	− 29.74	1.06
2454049.705	− 6.76	0.31	2.57	4.56	− 23.58	0.94
2454051.726	− 2.64	0.34	5.83	2.91	− 17.83	0.86
2454083.692	− 6.69	0.32	9.08	3.23	− 24.62	0.90
2454120.634	− 13.24	0.36	5.01	3.21	− 2.39	2.28
2454121.598	− 11.41	0.38	2.45	4.54	− 26.87	1.18
2454314.887	2.58	0.43	7.45	4.08	5.91	0.85
2454316.899	0.01	0.30	− 4.08	3.95	2.52	0.70
2454319.876	− 2.22	0.38	− 5.89	4.15	− 5.78	1.00
2454528.522	8.31	0.30	2.81	4.19	− 4.05	0.59
2454705.921	2.68	0.75	1.06	7.04	12.38	1.52
2454706.899	5.52	1.15	0.97	10.95	20.36	1.86
2454707.903	5.78	0.36	− 5.09	4.06	5.36	0.88
2454710.887	8.03	0.37	− 1.72	4.05	6.18	0.92
2454732.763	− 1.56	0.38	11.30	4.26	− 11.82	0.85
2454736.806	4.84	0.40	4.17	4.06	10.37	0.81
2454738.849	4.32	0.62	9.14	5.51	16.83	1.49
2455025.910	4.28	0.39	4.66	4.44	30.61	1.31
2455040.898	3.24	0.72	− 17.95	7.64	45.73	1.71
2455041.897	− 2.19	0.37	− 17.80	3.67	36.22	1.15
2455043.900	− 4.94	0.51	− 15.84	4.77	26.34	0.97
2455045.888	− 10.79	0.40	2.92	4.13	11.03	0.86
2455046.847	− 10.30	0.41	− 4.47	4.96	5.62	0.86
2455067.891	7.31	0.26	3.39	3.60	15.37	0.97
2455068.893	9.87	0.38	− 2.65	4.35	22.54	1.13
2455070.906	9.67	0.30	4.14	3.51	32.70	1.39

Table B1 – *continued*

Time (BJD)	RV (m s⁻¹)	RVerr (m s⁻¹)	CRX	CRXerr	DLW	DLWerr
2455073.884	11.14	0.30	− 1.26	3.84	44.13	1.39
2455075.872	6.72	0.37	− 16.64	3.87	50.61	1.66
2455103.812	1.93	0.51	− 1.68	4.78	19.72	1.20
2455108.791	4.44	0.42	3.61	3.63	21.62	1.15
2455110.770	4.17	0.89	8.21	8.08	39.61	1.85
2455112.790	2.58	0.31	− 6.26	3.81	26.84	1.00
2455115.784	− 3.03	0.39	− 11.45	4.39	27.77	1.01
2455122.775	− 5.81	0.36	− 8.17	3.98	2.36	0.75
2455124.781	− 4.63	0.24	1.80	3.17	− 2.51	0.56
2455128.793	− 1.94	0.32	0.08	3.45	− 9.62	0.71
2455133.765	5.24	0.38	− 0.69	4.31	4.99	0.81
2455137.765	1.77	0.27	− 6.96	3.22	2.45	0.63
2455141.675	2.71	0.30	0.54	3.00	1.56	0.66
2455164.591	− 0.01	0.26	− 2.67	2.87	6.32	0.54
2455167.579	3.62	0.24	− 4.53	2.96	0.17	0.61
2455169.584	3.56	0.27	− 4.67	2.72	3.03	0.61
2457741.706	0.39	0.85	11.10	5.43	− 6.29	0.43
2457743.716	− 1.79	0.82	− 4.01	3.86	0.19	0.37
2457744.741	− 2.08	0.85	− 5.14	3.75	3.68	0.34
2457747.711	− 7.32	0.85	− 6.96	7.55	7.98	0.70

Table B2. PFS RVs and stellar activity indicators.

Time (BJD)	RV (m s⁻¹)	RVerr (m s⁻¹)	S_{HK}	$S_{H\alpha}$
2455198.63	2.57	1.01	0.3248	0.0448
2455198.632	1.12	1.06	0.3323	0.0446
2455430.896	5.98	0.98	0.3078	0.0436
2455586.569	1.78	0.88	0.3021	0.043
2455785.851	− 5.61	0.94	0.2822	0.0432
2455790.843	− 5.72	1.13	0.3158	0.0434
2455793.883	− 4.14	1.2	0.3166	0.0439
2455795.922	− 4.12	1.21	0.3041	0.0446
2456141.926	5.18	1.14	0.3	0.0436
2456284.62	3.3	0.79	0.4561	0.0431
2456293.63	− 4.64	0.78	0.2864	0.0433
2456345.527	4.01	1.28	0.379	0.0431
2456501.925	− 1.79	1.09	0.31	0.0431
2456548.858	0.56	1.07	0.353	0.043
2456551.837	− 0.14	1.67	0.3521	− 1.0
2456556.829	5.31	1.05	0.2892	0.0444
2456604.679	− 2.71	0.81	0.3013	0.0433
2456607.721	− 10.12	0.92	0.2989	0.0433
2456611.744	− 4.62	0.89	0.3015	0.044
2456612.677	− 3.89	0.89	0.2927	0.0434
2456692.543	1.5	0.95	0.3021	0.0431
2456694.559	0.22	0.94	0.2835	0.044
2456698.547	− 0.43	1.06	0.3025	0.043
2456866.897	− 2.74	1.15	0.2999	0.043
2456871.905	− 1.55	1.03	0.2838	0.0432
2456877.917	2.74	1.15	0.3891	0.0432
2457022.633	− 3.35	0.77	0.2926	0.0432
2457027.631	− 0.38	0.83	0.2914	0.0441
2457052.553	− 2.92	0.88	0.294	0.0432
2457064.54	− 3.2	1.0	0.3909	0.0434
2457260.897	− 0.05	1.07	0.3124	0.0426
2457267.853	− 0.25	1.04	0.302	0.0434
2457319.787	− 5.37	0.93	0.2985	0.0433
2457323.797	− 7.37	0.93	0.3067	0.0435
2457389.609	− 7.63	0.88	0.2894	0.0432
2457616.915	6.98	1.09	0.2939	0.0432
2457626.922	10.73	1.08	0.2881	0.0439
2457737.648	4.36	0.84	0.3004	0.0428

Table B2 – *continued*

Time (BJD)	RV (m s⁻¹)	RVerr (m s⁻¹)	S_{HK}	$S_{H\alpha}$
2457740.613	9.51	0.82	0.2833	0.0426
2457759.556	− 0.92	0.8	0.2854	0.0434
2457764.59	11.8	0.82	0.3011	0.0446
2457768.579	8.34	0.78	0.4384	0.043
2458356.871	− 5.48	0.92	0.4683	0.044
2458356.875	− 3.03	0.88	0.4652	0.0436
2458407.77	3.76	0.8	0.4698	0.0438
2458411.721	5.37	0.85	0.5125	0.0442
2458411.725	5.77	0.86	0.5218	0.0442
2458417.721	7.72	0.85	0.4847	0.0435
2458467.651	− 5.51	0.76	0.4517	0.0437
2458467.655	− 5.26	0.71	0.4517	0.0438
2458467.783	− 5.5	0.78	0.4466	0.0432
2458467.787	− 3.34	0.75	0.4498	0.0432
2458468.626	− 2.48	0.8	0.4711	0.0439
2458468.63	− 1.63	0.8	0.4622	0.0433
2458469.625	− 0.35	0.77	0.4671	0.044
2458469.629	0.87	0.72	0.4664	0.0435
2458469.751	1.03	0.74	0.4733	0.0434
2458469.755	− 0.03	0.74	0.47	0.0434
2458471.627	1.91	0.7	0.4681	0.0436
2458471.632	1.1	0.73	0.4598	0.0435
2458471.676	1.16	0.75	0.471	0.0439
2458471.68	2.36	0.69	0.4692	0.0439
2458472.606	1.16	0.71	0.4577	0.0439
2458472.61	1.78	0.71	0.4528	0.044
2458472.744	− 0.67	0.73	0.4651	0.0433
2458472.748	2.74	0.69	0.4856	0.0432
2458473.573	2.41	0.73	0.4722	0.0436
2458473.577	2.59	0.68	0.4666	0.0435
2458473.644	2.1	0.67	0.4589	0.0435
2458473.648	2.57	0.71	0.4567	0.0435
2458474.655	2.24	0.75	0.4628	0.0439
2458474.659	2.26	0.65	0.4545	0.0441
2458474.73	1.37	0.79	0.4861	0.0438
2458474.734	2.25	0.83	0.4906	0.0439
2458475.587	2.31	0.68	0.4641	0.0435
2458475.591	3.17	0.69	0.4668	0.0436

Table B2 – *continued*

Time (BJD)	RV (m s^{-1})	RVerr (m s^{-1})	S_{HK}	$S_{H\alpha}$
2458475.715	2.43	0.7	0.4658	0.0435
2458475.72	2.28	0.74	0.4712	0.0434
2458476.582	2.98	0.73	0.4705	0.0438
2458476.586	3.98	0.68	0.4685	0.0437
2458476.674	3.56	0.65	0.4646	0.0441
2458476.678	3.88	0.67	0.463	0.0441
2458479.607	9.91	0.66	0.4783	0.0436
2458479.611	9.78	0.66	0.4784	0.0437
2458479.747	10.16	0.78	0.5004	0.0436
2458479.751	9.1	0.76	0.513	0.0437
2458480.637	9.07	0.78	0.4949	0.0437
2458480.649	9.49	0.73	0.4956	0.0436
2458480.735	11.96	0.75	0.4928	0.0435
2458480.739	10.72	0.77	0.491	0.0435
2458501.532	− 8.46	0.7	0.4341	0.0428
2458501.536	− 7.72	0.81	0.4452	0.0428
2458501.61	− 9.73	0.74	0.4418	0.0428
2458501.614	− 7.92	0.73	0.4412	0.0428
2458502.522	− 9.63	0.75	0.431	0.0435
2458502.526	− 8.32	0.73	0.4293	0.0434
2458502.643	− 8.86	0.75	0.4298	0.0427
2458502.648	− 9.64	0.74	0.4395	0.0428
2458503.538	− 7.62	0.77	0.4269	0.0434
2458503.629	− 7.28	0.71	0.4408	0.043
2458503.633	− 7.18	0.74	0.4278	0.0429
2458504.623	− 7.13	0.74	0.4335	0.0428
2458504.627	− 6.97	0.72	0.4272	0.0429
2458504.679	− 7.13	0.74	0.4373	0.0429
2458504.683	− 5.61	0.7	0.4467	0.043
2458505.525	− 6.11	0.72	0.4303	0.043
2458505.529	− 7.0	0.73	0.4365	0.043
2458505.613	− 6.59	0.76	0.4448	0.043
2458505.617	− 6.66	0.83	0.4828	0.043
2458506.523	− 5.71	0.76	0.4496	0.0435
2458506.527	− 5.03	0.88	0.4612	0.0433
2458506.595	− 5.46	0.82	0.4818	0.0433
2458506.6	− 2.99	0.92	0.4843	0.0432
2458507.527	− 2.57	0.86	0.4613	0.0434
2458507.531	− 2.37	0.87	0.4851	0.0434
2458507.601	− 4.29	0.67	0.4231	0.043
2458508.523	− 1.87	0.74	0.4489	0.0428
2458508.528	− 3.87	0.84	0.4415	0.0428
2458508.652	− 2.17	0.93	0.4681	0.0432
2458508.657	− 2.91	0.83	0.4851	0.0432
2458509.523	− 1.25	0.89	0.4762	0.0432
2458509.527	− 1.49	0.87	0.4796	0.0431
2458510.524	1.34	1.02	0.4926	0.0433
2458510.528	0.62	1.02	0.5029	0.0432
2458511.521	0.06	0.79	0.4574	0.0436
2458511.525	− 0.66	0.77	0.4573	0.0435
2458526.526	− 5.53	0.96	0.5108	0.0431
2458526.53	− 2.79	0.86	0.4894	0.0429
2458527.514	− 3.71	1.04	0.4926	0.0435
2458527.519	− 5.36	0.98	0.5053	0.0434
2458527.647	− 0.58	1.19	0.5673	0.0428
2458527.652	− 2.91	1.15	0.5594	0.0424
2458528.516	− 4.36	0.9	0.4705	0.0434
2458528.52	− 1.56	0.91	0.4669	0.0434
2458528.583	− 3.25	0.94	0.4535	0.0435
2458528.587	− 4.76	1.02	0.489	0.0434
2458529.521	− 3.44	0.92	0.4432	0.0429
2458529.525	− 4.82	0.95	0.4466	0.043
2458529.599	− 4.89	0.9	0.4597	0.0433
2458529.603	− 3.59	0.93	0.4628	0.0433
2458530.511	− 2.51	0.98	0.4602	0.0428

Table B2 – *continued*

Time (BJD)	RV (m s^{-1})	RVerr (m s^{-1})	S_{HK}	$S_{H\alpha}$
2458530.515	− 5.21	0.92	0.4546	0.0429
2458530.585	− 7.03	0.92	0.4452	0.0428
2458530.59	− 5.35	0.88	0.4662	0.0427
2458531.604	− 5.22	0.87	0.4642	0.0424
2458531.609	− 5.12	0.88	0.4789	0.0424
2458532.513	− 5.5	0.89	0.4558	0.0431
2458532.517	− 3.41	0.89	0.4712	0.0429
2458532.604	− 5.96	0.96	0.4772	0.0429
2458532.608	− 4.94	0.9	0.4657	0.0429
2458674.921	− 5.03	0.89	0.4512	0.044
2458676.921	− 5.15	1.16	0.4791	0.0435
2458676.928	− 5.0	0.93	0.4381	0.0437
2458677.893	− 4.72	0.99	0.4588	0.0441
2458677.897	− 2.52	1.0	0.4617	0.0441
2458678.892	− 4.82	0.92	0.4558	0.044
2458678.896	− 2.29	0.99	0.4536	0.0441
2458681.894	2.27	1.18	0.5196	0.0442
2458681.898	1.65	0.99	0.4938	0.0445
2458683.905	1.99	0.95	0.46	0.0433
2458683.914	− 0.32	0.92	0.4505	0.0439
2458684.869	− 2.07	0.85	0.4488	0.0439
2458684.873	− 1.68	0.88	0.4473	0.0439
2458709.922	− 0.56	0.9	0.45	0.0436
2458709.927	− 1.05	0.91	0.4488	0.0437
2458737.78	7.85	1.14	0.4805	0.0437
2458737.873	9.19	1.1	0.4961	0.0436
2458737.877	7.22	1.18	0.5039	0.0438
2458738.75	2.55	0.97	0.4954	0.0438
2458738.754	3.93	1.13	0.4903	0.0438
2458738.88	3.64	1.09	0.4989	0.0441
2458738.883	2.18	1.12	0.5169	0.0442
2458738.888	3.6	1.1	0.517	0.0441
2458739.776	2.97	0.97	0.482	0.0441
2458739.869	1.24	0.98	0.4715	0.0436
2458740.776	1.91	0.95	0.4771	0.0437
2458740.862	0.29	0.94	0.4793	0.0437
2458741.782	− 0.62	0.99	0.4868	0.0435
2458741.785	1.9	1.04	0.4875	0.0436
2458744.796	0.54	1.06	0.4922	0.0435
2458744.799	− 1.16	1.1	0.4903	0.0435
2458744.874	− 0.94	1.02	0.4625	0.0435
2458760.775	0.3	0.87	0.4255	0.0441
2458760.846	1.18	0.91	0.4308	0.044
2458761.847	− 0.92	0.87	0.4285	0.0435
2458762.762	− 0.67	0.94	0.4483	0.0433
2458762.767	0.94	0.97	0.4491	0.0435
2458762.838	0.0	0.96	0.4431	0.0434
2458762.842	− 1.69	0.92	0.4394	0.0435
2458763.804	1.27	0.8	0.406	0.044
2458764.766	2.41	0.92	0.4494	0.0438
2458764.77	3.0	0.89	0.4498	0.0439
2458764.837	2.53	0.91	0.4642	0.0433
2458764.842	2.9	0.93	0.4482	0.0434
2458766.757	7.0	0.84	0.4269	0.0436
2458766.839	5.87	0.78	0.4332	0.0433
2458767.752	8.35	0.86	0.4398	0.0441
2458768.764	8.85	0.89	0.4857	0.0442
2458768.839	10.45	0.87	0.4452	0.0437
2458828.579	5.06	0.71	0.4599	0.0433
2458828.586	6.45	0.74	0.4904	0.0433
2458828.657	5.66	0.72	0.5039	0.0434
2458828.661	5.7	0.78	0.4898	0.0434
2458829.726	7.66	0.9	0.4901	0.0433
2458829.73	8.43	0.9	0.5023	0.0434
2458831.616	7.26	0.83	0.4886	0.0433

Table B2 – *continued*

Time (BJD)	RV (m s^{-1})	RVerr (m s^{-1})	S_{HK}	$S_{H\alpha}$
2458831.621	7.08	0.75	0.4865	0.0434
2458831.702	6.87	0.81	0.4915	0.0433
2458831.705	6.82	0.78	0.5013	0.0434
2458832.584	5.69	0.89	0.5113	0.0428
2458832.589	7.38	0.82	0.4735	0.043
2458832.625	6.62	0.98	0.4884	0.0432
2458832.632	5.63	0.91	0.4933	0.0431
2458833.621	5.57	0.84	0.4904	0.0433
2458833.625	3.27	0.87	0.4919	0.0433
2458833.689	6.29	0.91	0.4978	0.0431
2458833.693	6.03	0.79	0.4841	0.0432

Table B2 – *continued*

Time (BJD)	RV (m s^{-1})	RVerr (m s^{-1})	S_{HK}	$S_{H\alpha}$
2458834.603	2.7	0.83	0.4851	0.0434
2458834.606	3.74	0.83	0.4849	0.0435
2458834.677	3.58	0.83	0.4732	0.0435
2458834.681	2.03	0.84	0.4549	0.0433
2458837.651	0.38	0.85	0.4765	0.0434
2458837.655	0.09	0.85	0.4666	0.0436
2458887.535	− 6.62	1.06	0.4883	0.0443
2458887.539	− 5.47	0.92	0.5091	0.0442

This paper has been typeset from a TEX/LATEX file prepared by the author.